8-2017

Optimization of Miniaturized Resonant Microwave Cavities for Use in Q-Thrusters

Joshua Steven Pennington
University of Arkansas, Fayetteville

Optimization of Miniaturized Resonant Microwave Cavities for Use in Q-Thrusters

A thesis submitted in partial fulfillment
of the requirements for the degree of
Master of Science in Microelectronics-Photonics

by

Joshua Steven Pennington
Arkansas Tech University
Bachelor of Science in Physics, 2015
Arkansas Tech University
Bachelor of Science in Mechanical Engineering, 2015

August 2017
University of Arkansas

This thesis is approved for recommendation to the Graduate Council.

Dr. Adam Huang
Thesis Director

Dr. Magda El-Shenawee
Committee Member

Dr. William Harter
Committee Member

Dr. Rick Wise
Ex-Officio Member

The following signatories attest that all software used in this thesis was legally licensed for use by Joshua Steven Pennington for research purposes and publication.

Mr. Joshua Steven Pennington, Student	Dr. Adam Huang, Thesis Director

This thesis was submitted to http://www.turnitin.com for plagiarism review by the TurnItIn company's software. The signatories have examined the report on this thesis that was returned by TurnItIn and attest that, in their opinion, the items highlighted by the software are incidental to common usage and are not plagiarized material.

Dr. Rick Wise, Program Director	Dr. Adam Huang, Thesis Director

Abstract

A gedankenexperiment was considered to compare a hypothetical thruster that used no reaction mass to propulsion methods currently in use. A brief discussion of previous research work done on closed resonant cavity thrust devices was conducted. Using the previous work as a template, a simulation plan was devised. Computational models of resonant microwave cavities were constructed and investigated using COMSOL software. These COMSOL simulations were verified against known analytical solutions using Matlab software as a computational tool. Multiphysics simulations were created to study the microwave heating environment of the resonant cavities. From the COMSOL study outputs, the electromagnetic field magnitude, temperature, surface resistive losses, volume resistive losses, quality factor, and energy contained in the electric field were presented and discussed. The disagreements between the computational model and real-world resonant cavities were also presented and discussed.

Acknowledgement

I would like to acknowledge my research group colleagues Morgan Roddy and John Lee for their guidance and being there when you need someone to bounce an idea off. The mentorship of my research instructor, Dr. Adam Huang, has been phenomenal. His contribution to the success in my research career cannot be overstated.

I would like to thank the University of Arkansas as an institution for providing the resources and environment necessary to conduct meaningful research. I also want to acknowledge the Microelectronics-Photonics program, the Mechanical Engineering department, and the Graduate School for supporting me financially during my tenure as a graduate student.

A special thanks to Dr. Rick Wise and Renee Jones-Hearon. Without their help, I'm not sure if any student would be able to successfully navigate the ins and outs of graduate school. I certainly wouldn't have made it.

Dedication

This is dedicated to all the educators that had a hand in shaping my life for the better. Your guidance helped set me on a path that has led to the career of my dreams and hopefully one day will lead to the stars. I couldn't have done this without you.

To my parents, the household you built fostered a love for creativity, a desire to seek out more understanding, and respect for the importance of hard work. I couldn't have done this without you.

For Haley, my partner, my confidante, my love. I couldn't have done this without you.

Table of Contents

List of Figures:

List of Tables

Chapter 1: Introduction

1.1 Motivation

One of the unique challenges that engineers working in a space environment face is the immense distances between celestial bodies. The large distances require that propulsion systems and their components make up a large majority of the weight of the system. This is due to a defining characteristic of travel in space expressed in the famous Tsiolkovsky rocket equation:

$$\Delta v = v_e * \ln(\frac{m_2}{m_1}) \qquad \text{(Equation 1.1.1)}$$

where Δv is the change in velocity, v_e is the velocity of the ejected fuel, and m_1 and m_2 are the initial and final mass of the spacecraft, respectively. All maneuvers in space require a change in velocity; the larger the change in velocity, the more a spacecraft can change its course. If all fuel was used in a single maneuver, the masses seen in the natural logarithm would be the fraction of the spacecraft without fuel to that of the spacecraft with fuel. The most maneuverable spacecraft would have a very high exhaust velocity and a very high mass fraction. These limitations lead to limited weight budgets for instrumentation, power systems, life support, and any other part of the spacecraft that does anything but move you around. The largest rocket ever launched is the Saturn V. It weighed 6.5 million lbs. when fully fueled for a lunar mission, but the payload delivered to lunar orbit was designed to weigh 90,000 lbs. [1]. The final delivered payload composed only ~1.4% of the weight of the initial rocket. This is the requirement of Newton's Third Law. To go anywhere in space, you must eject mass to impart momentum to your spacecraft. Excepting photon radiation pressure propulsion, all current propulsion methods carry their reaction mass as fuel on the spacecraft [2]. The method by which the propulsion system accelerates the fuel is how propulsion systems are classified. Propulsion systems can be

classified into these categories: chemical propulsion, electric propulsion, pressurized gas propulsion, and photon radiation pressure propulsion [3], [4].

Together, these types of propulsion must be combined to meet all mission requirements of a spacecraft. These include orbital launch, orbital adjustments, spacecraft orientation, and station keeping. Large chemical rockets are used for launch. Their huge thrust is necessary to accelerate out of Earth's gravity well and up to orbital velocities [1]. Chemical propulsion is also used when it is needed to accelerate a large mass to a high velocity. Satellites delivered to orbit rely on a variety of propulsion options to tend degrading orbits, re-task to different orbits, and point the spacecraft [3], [5]–[7]. These include chemical monopropellant or bipropellant thrusters, pressurized gas thrusters, and electric propulsion systems. For interstellar probes, electric propulsion has become a competitor for main propulsion systems. Examples of propulsion systems used on long range spacecraft are bi-propellant engines like the Leros-1b aboard the Juno spacecraft currently in orbit of Jupiter [8]. The International Space Station also uses a bipropellant engine in order to keep its orbit from degrading [9]. Spacecraft such as Hayabusa, SMART-1, and the Soviet Meteor class of weather satellites have also used electric propulsion to serve as main propulsion systems and to enhance mission capabilities [10]–[13]. Pressurized gas systems are also in use in satellites for maneuvering and pointing and were even used in the Manned Maneuvering Unit that astronauts used to maneuver in space [14]–[16].

Chemical rockets use the energy of a chemical reaction (combustion, catalytic, or otherwise) to propel exhaust mass and produce thrust. Pressurized gas propulsion systems use the energy of the pressure difference between the exhaust and the plenum of the thruster to impel their spacecraft. Gas systems are sometimes electrically enhanced to increase the energy in their projected fuel [14], [17], [18]. Electric propulsion systems of all types use a potential difference

to accelerate particles that interact with the electric field. Fuel for electric propulsion systems comes in all types; Xenon, ionic liquids, solid Teflon, and many other types of fuels have been used in the past. The method and operation of electric propulsion systems is highly varied [2], [10]–[12], [19]–[29]. The efficiency of different propulsion methods varies and is quantified by their specific impulses, I_{sp}., which has a units of seconds (s). Pressurized gas systems see efficiencies of around 100 s, while electric propulsion systems may be as high as 10,000 s [2], [14], [30], [31]. As stated before, regardless of acceleration method, all of these propulsion methods require fuel. Because of this, they all have a limited possible amount of motive power available to them. There is no way to refill a spacecraft's fuel tanks. When the fuel runs out, the spacecraft ceases to be able to maneuver, correct degrading orbits, or adjust orbital parameters. Thus, every spacecraft has a limited amount of time before it becomes inoperative.

A driving force in spacecraft development is the extension of the longevity of spacecraft. For scientific, engineering, mission planning, and economic reasons it is desirable to increase the amount of time that a spacecraft's propulsion systems can operate. This leads to the conclusion that the ideal hypothetical propulsion system is one that doesn't require fuel to produce thrust and that can produce thrust as long as whatever motive power the thruster relies on is available. The interest in developing propulsion systems that require no fuel drove the research into radiation pressure propulsion systems like solar sails and photon rockets. A solar sail aboard the LightSail CubeSat was tested in 2015 [32]. A major operational limitation of these propulsion methods is the extremely low amounts of thrust they produce. Their thrust production is also highly dependent on the photon pressure in the area of space the solar sail occupies, the farther away from the sun, the lower the thrust.

Another type of device that potentially meets the qualification of producing thrust with

no reaction mass is the Quantum Vacuum Plasma Thruster (Q-thruster) or Electromagnetic (EM) Drive. Q-thrusters appear to produce thrust only from electrical power. They consist of a sealed microwave cavity driven by an antenna emitting at the resonant frequency of the cavity. These devices have been tested by several laboratories and all tests have shown a positive result of thrust production [33]–[38]. It should be noted immediately that only preliminary research has been done on these devices. There has been no well-developed theory of operation published that describes the physical means by which the devices produce thrust and the option of experimental error causing the thrust readings is still a possibility. Despite the uncertain nature of the state of the research at its current point, the opportunity represented by a thruster that requires no fuel requires that the phenomena be studied regardless of the explanation being spurious or impactful.

For these reasons, the study of resonant microwave cavities for use in Q-thrusters was chosen as the topic of investigation for this thesis.

1.2 Background

As highlighted in the Motivation section, the concept of a thruster that requires no fuel would alleviate many of the operational limitations that affect contemporary spacecraft. This has attracted interest from several research and commercial entities internationally. The commercial entities are Cannae LLC (www.cannae.com) out of Philadelphia, PA and Satellite Propulsion Research (SPR) Ltd (www.emdrive.com) out of Aldermaston, U.K. The research laboratories that have performed tests on the EM Drive/Q-thruster technologies are the Eagleworks Labs of NASA Johnson Space Center in Houston, TX, the research group led by Martin Tajmar (https://tu-dresden.de/ing/maschinenwesen/ilr/rfs/die-professur/inhaber-in) at the Institute of Aerospace Engineering, Technische Universität (TU) Dresden, Germany, and the research group led by Yang Juan (http://teacher.nwpu.edu.cn/en/yangjuan.html) at the Northwestern

Polytechnical University (NWPU) in Xi'an, China. The state of the research is still very open ended. To date, all organizations who have published their findings have shown that the devices produce thrust [33]–[35], [37]–[39]. However, there has only been one paper that has gone through the peer review process [34]. This dearth of data has led to many open scientific questions: Is thrust really being produced? What is the mechanism for producing that thrust? What geometrical, electromagnetic, and material properties affect thrust production? These engineering design parameters are all poorly understood. Much of the reason why the phenomenon is poorly understood after more than a decade after initial reporting is because much of the work being done is proprietary. The responding scientific research has mostly been done as a verification of the designs created by both companies.

Figure 1.1 - Resonant cavity "Q-thruster" built and tested by NASA Eagleworks.

The phenomena of a sealed microwave resonant cavity producing thrust were first reported by Roger Shawyer [39]. Based on this idea he founded the company SPR Ltd. Shawyer designed and built the first prototype EM Drive cavities that were shaped like a frustum, a truncated cone. This design is the most commonly tested design. It has been used in experiments by NASA Eagleworks, The Technische Universität Dresden, and China's Northwestern

Polytechnical University [33]–[35], [37], [38]. Shawyer's design geometry was used directly in the work done by NASA Eagleworks labs, and with altered dimensions by Tajmar and Juan [34], [35], [37], [38]. The resonant cavity used by NASA Eagleworks is shown in Figure 1.1 [34].

This thesis' work is also based on the original frustum design. Roger Shawyer hypothesizes that a "radiation pressure imbalance" on the interior of the cavity produces thrust [39]. Another commercial entity developing an electromagnetic thruster is Cannae LLC; they have never published research on their work. The only public record of their thruster design is a patent filed in 2011 [40].

Other labs that have released a single paper on the topic of resonant microwave cavity thrusters are Juan, and Tajmar [37], [38]. Both investigators used magnetrons to drive their cavities and a knife-edge balance to measure the thrust. Tajmar reported thrusts of tens of μN for an input power of 700 W. Juan reported a thrust of hundreds of mN for an input power of 1 kW [38]. The thrust results have radically different orders of magnitude for similar input powers. Tajmar reasons that this is due to the difference in quality factor between the two experiments [37]. The cavity built by TU Dresden only had a quality factor (defined in Equation 2.3.5.1) of 50, while the cavity built by the NWPU had a quality factor of ~40,000. It must be noted that the report by Juan was published through an internal journal for the university where the laboratory is located and that no other thrust test published since then has had thrust:power ratios as high.

The majority of academic research that has been completed has been by the Eagleworks Advanced Propulsion Laboratories at NASA Johnson Space Center in Houston, TX. The lab has been investigating the topic of resonant cavity microwave thrusters since its inception in 2005 [41]. Since then the lab has presented their findings at conferences and were recently published in the peer reviewed Journal of Propulsion and Power [33]–[35]. The head of NASA Eagleworks

Labs, Dr. Sonny White, has hypothesized that the thrust occurs due to an interaction with the virtual particles that make up the quantum vacuum Their latest findings were measured under hard vacuum on an extremely sensitive torsion balance thrust stand capable of resolutions of ± 0.1 μN. The labs report a thrust density of 1.2 mN/kW [34]. To compare to contemporary electric propulsion options, the Hayabusa spacecraft uses ion engines that output 24 mN of thrust for 1.05 kW of power. These thrust output levels are only different by an order of magnitude. If thrust tests for Q-thrusters continue to be validated and understanding of the operation of the device can be developed to increase the thrust output by an order of magnitude, the field of in-space propulsion would be revolutionized.

Chapter 2: Experimental Methods

2.1 COMSOL Comparison to Analytical Models

The models that are the final focus of this investigation are all complex and have no analytical solution. In order to verify COMSOL's solver methods in relation to known analytical solutions, the cases of perfectly conducting rectangular, cylindrical, and spherical cavities were considered [42]. Additionally, this exercise was undertaken in order to gain an understanding of the use of COMSOL's RF module. These geometries all have analytical solutions to Maxwell's equations that can be compared to the computationally generated COMSOL solutions. The solutions for these geometries are as follows:

Rectangular: $E_z(x,y,z) = A * \sin\left(\frac{m*\pi*x}{a}\right) * \sin\left(\frac{n*\pi*y}{b}\right) * \cos(\frac{l*\pi*z}{h})$ (Equation 2.1.1)

Cylindrical: $E_z(r,z) = A * J_0\left(\frac{\xi_n*r}{a}\right) * \cos(\frac{l*\pi*z}{h})$ (Equation 2.1.2)

Spherical: $E_z(r) = A * J_n(r)$ (Equation 2.1.3)

In all analytical solutions, A is a scalar normalization constant. For the rectangular solutions, the size of the cavity in the x, y, and z directions is a, b, and h respectively. The modal indices m, n, and l represent the indices of the transverse electric mode. The cylindrical solution is simplified to two independent variables, r and z. The variable r is the vector addition of the x and y coordinates at a specific height z. The function J_0 is the Bessel function of the zeroth order and is evaluated at the product of $\frac{\xi_n*r}{a}$. The variable a is the radius of the cylinder and ξ_n is the nth order root of the zeroth order Bessel function. This term serves to modulate the radial intensity of the equation to the behavior of the nth order Bessel function. Because the cylindrical solution is

only dependent on two variables, the modal indices are n and l. The spherical solution is only dependent on the variable r, which is the vector addition of input values x, y, and z. The solution takes the form of the spherical Bessel function

Solutions were calculated using Matlab scripts that can be found in Appendix A. The COMSOL computed results were imported into Matlab. These data include the location that COMSOL computed a result at, and the result at that point. The location data from COMSOL can be modified in several ways. For these verification tests, two location output data types were used. One used a three-dimensional regular grid output of the geometry, the other used the locations of the tetrahedral mesh intersections. The locations output from COMSOL were used directly in the analytical solutions presented in Equations 2.1.1, 2.1.2, and 2.1.3. The set of data from COMSOL and the set of data from the analytical solutions were then compared to each other. The tetrahedral outputs are the points where COMSOL directly computes the electric field, while the grid outputs require interpolation between those points. The analytical solutions to the cavities' eigenfrequencies were then compared to COMSOL solutions.

A characteristic of the COMSOL eigenfrequency study that must be noted is that in the solution for the electric field, it will arbitrarily choose a magnitude to normalize to. This is due to the nature of the sparse solver used in the computations. The sparse solver will converge to a solution at a single point in the computational space of the model. From there, this solution with an arbitrary magnitude will "spread" out through tetrahedrons surrounding that point in an organic manner. This arbitrary normalization constant in the COMSOL solutions requires that the Matlab script be renormalized to the same constant. Once the Matlab solutions were renormalized to the same levels as the COMSOL solutions, the nature of the data output from COMSOL allowed for each calculated point to be directly compared against each other. This

allowed for the percent difference to be calculated between each point on all sets of data and then plotted. The mean percent difference for all points compared between COMSOL and the analytical solutions is presented in Table 2.1.1 and plots showing the collection of data that these means were taken from is shown in Figures 2.1.1, 2.1.2, and 2.1.3.

Table 2.1.1 - Comparison between COMSOL generated and analytical solutions to resonant EM Cavities.

	Number of Points	Mean Percent Difference	Standard Deviation
Rectangular Cavity Mesh Output	3122	0.0006	0.0176
Rectangular Cavity Grid Output	1000000	0.0040	0.0710
Cylindrical Cavity Mesh Output	1277	0.0005	0.0091
Cylindrical Cavity Grid Output	1000000	0.0015	0.0060
Spherical Cavity Mesh Output	19792	-0.4049	0.5305
Spherical Cavity Grid Output	1000000	-0.0210	0.6722

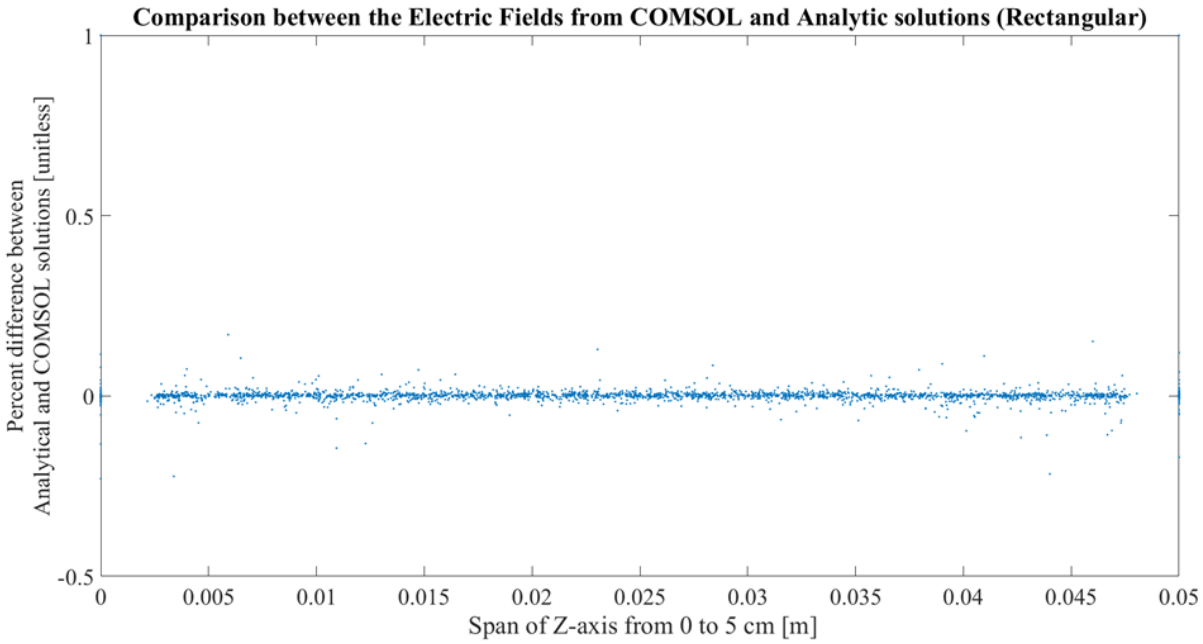

Figure 2.1.1 - Percent difference comparison between all COMSOL points and analytical solutions for a rectangular resonant cavity.

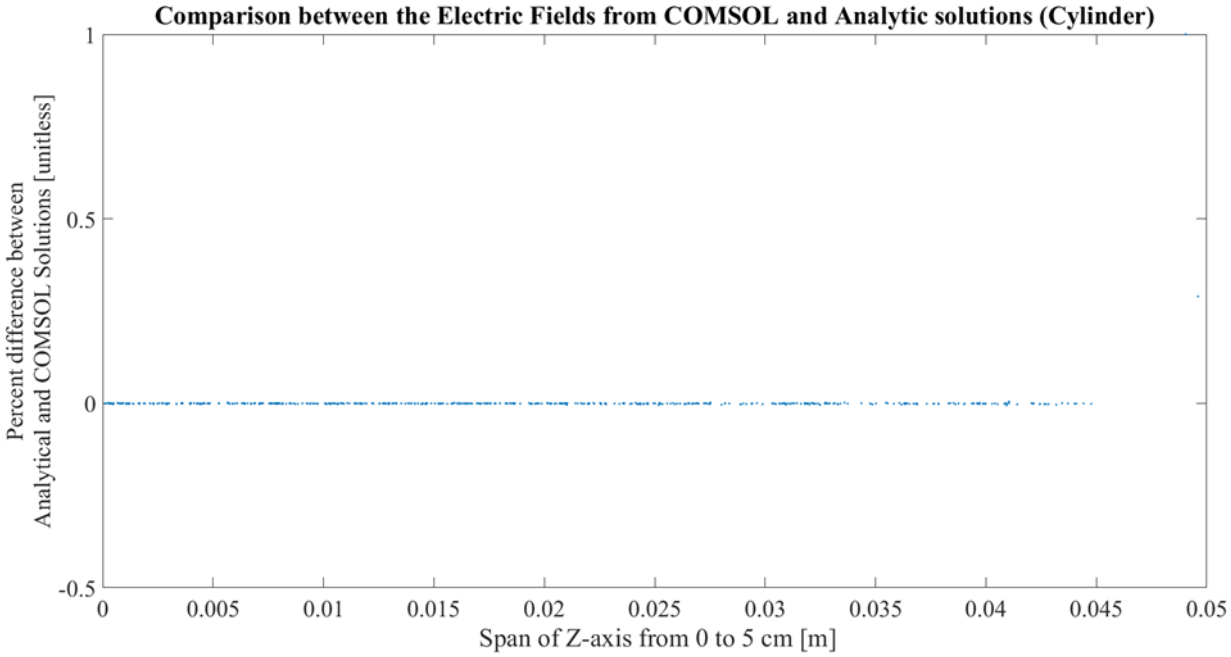

Figure 2.1.2 – Percent difference comparison between all COMSOL points and analytical solutions for a cylindrical resonant cavity.

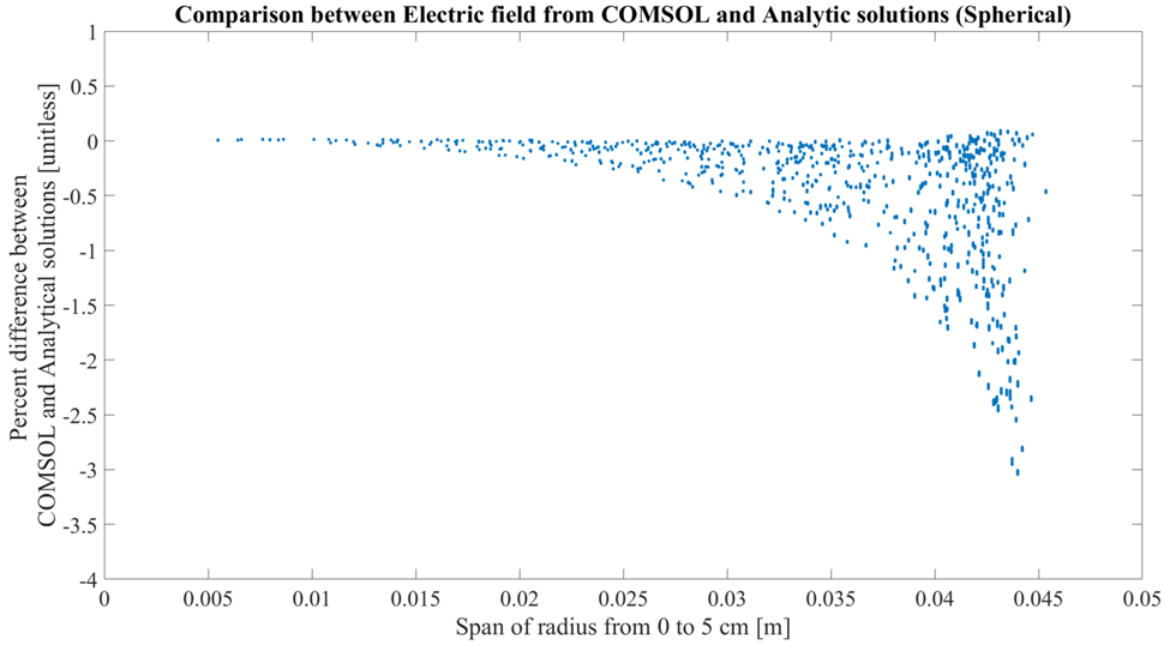

Figure 2.1.3 - Percent difference comparison between all COMSOL points and analytical solutions for a spherical resonant cavity.

From Table 2.1.1 and Figure 2.1.4, it is apparent that the spherical cavity's analytical solutions do not compare as closely as the solutions for the rectangular and cylindrical cavities. As can be seen in the figure, the disagreement between the two solution sets increases toward the boundary of the spherical cavity, at maximum the disagreement is ~320%. This disagreement exists because the COMSOL solution does not completely match the analytical solution. The COMSOL output can be seen to be smeared across a range of answers not matched by the spherical Bessel function. This behavior is displayed in Figure 2.1.4 and shows that while the COMSOL generated solution diverges highly from the analytically predicted solution, their behavior closely resembles each other.

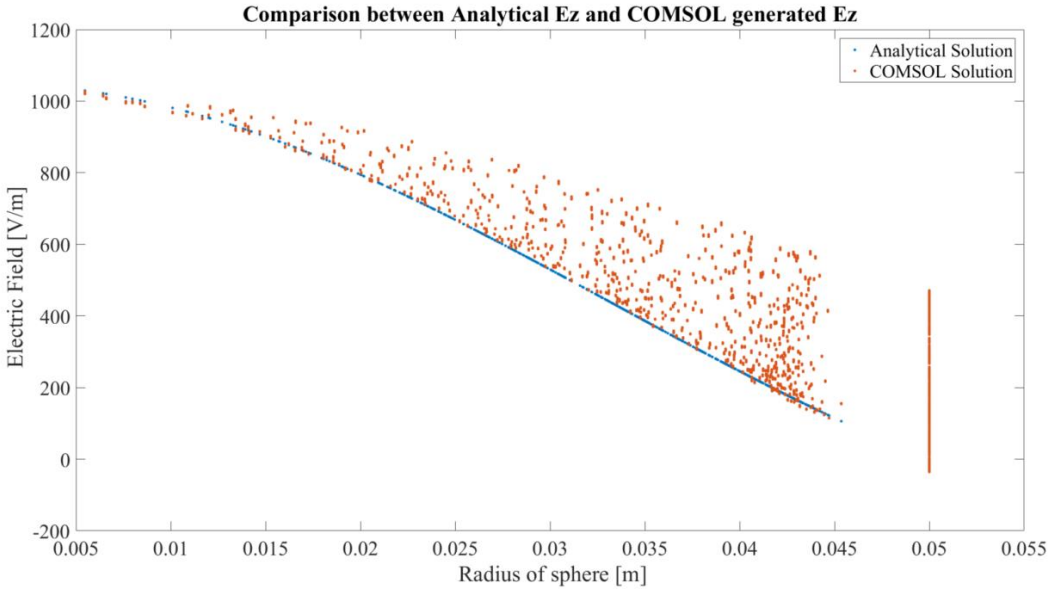

Figure 2.1.4 - COMSOL generated and analytically solved solutions to the z-component of the electric field for a spherical resonant cavity.

In an attempt to resolve the disagreement between the spherical analytical solution and the COMSOL solution, several separate analyses were performed on the data. One attempt was based on changing the density of the mesh used in the Eigenstudy. The simulation was ran with

mesh densities ranging between ~1100 domain mesh elementals and ~250000 domain mesh elements. In all completed simulations, the spread in data was equal to that seen in Figure 2.1.4. Other attempts to resolve the disagreement included isolating planar data (xy-plane, xz-plane, and yz-plane) and altering the solver settings used in COMSOL. None of these attempts led to a change in the spread of data that is apparent in Figure 2.1.4. The lack of change in the data set even after manipulation leads to the belief that COMSOL's Eigenstudy does not directly compute the electric field in the geometry by directly solving Maxwell's equations, but instead relies on some non-physical overlay to create arbitrary form factors for the electric field within resonant cavities. It is not expected that the failure to accurately compare COMSOL's spherical resonant cavity model to that represented by the analytical solution will affect the cavities that are the focus of this thesis. The solvers used to simulate the frustum shaped resonant cavities are more tightly related to the physical models that they represent.

From the eigenfrequency determined from the computational models of the cylindrical and rectangular resonant cavities, a micropatch antenna was designed using the Matlab script in Appendix B. This antenna was then modeled as the feed antenna into the cylindrical and rectangular cavities. The purpose of this exercise was to determine if the micropatch driven cavities could support modes that were highly analogous to the analytical solutions. This was a concern due to the comparative sizes of the micropatch antennas to the cavities they were driving. The worry was that the field pattern emitted by the antenna would overpower the resonant mode of the cavity. The modeling shown in Figures 2.1.5 and 2.1.6 shows that the resonant cavity modes were replicated very closely to their analytical counterparts. Figure 2.1.5 shows the cylindrical cavity and Fig. 2.1.6 shows the rectangular cavity. Only the cylindrical and rectangular cavities were used because only they had flat surfaces to place antennas.

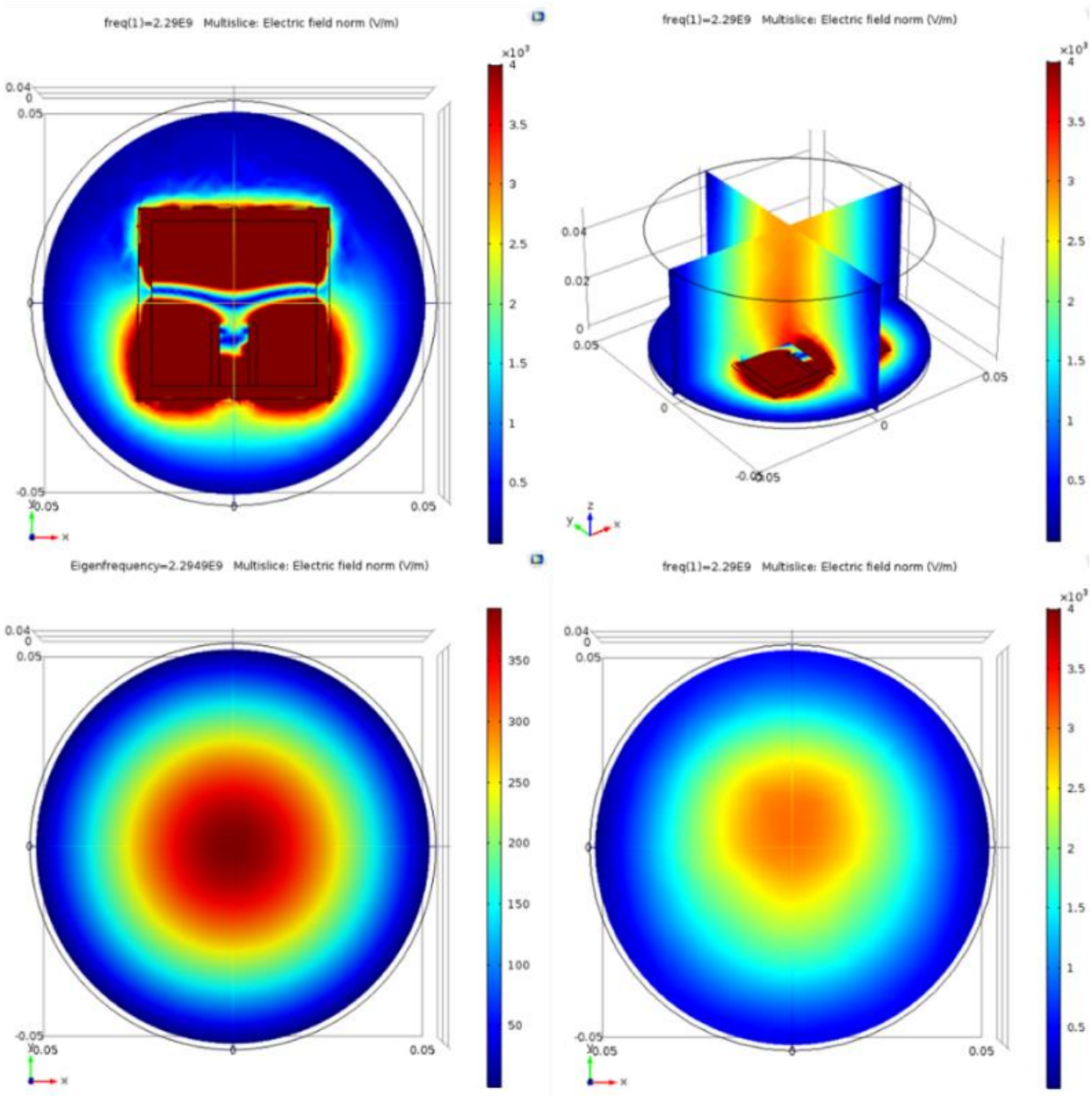

Figure 2.1.5 - a) A slice of the electric field at the antenna surface. b) A 3D view of the electric field in the cylindrical cavity. c) X-Y plane of the analytical eigenmode electric field. d) X-Y plane of the electric field in the cavity driven by a micropatch antenna

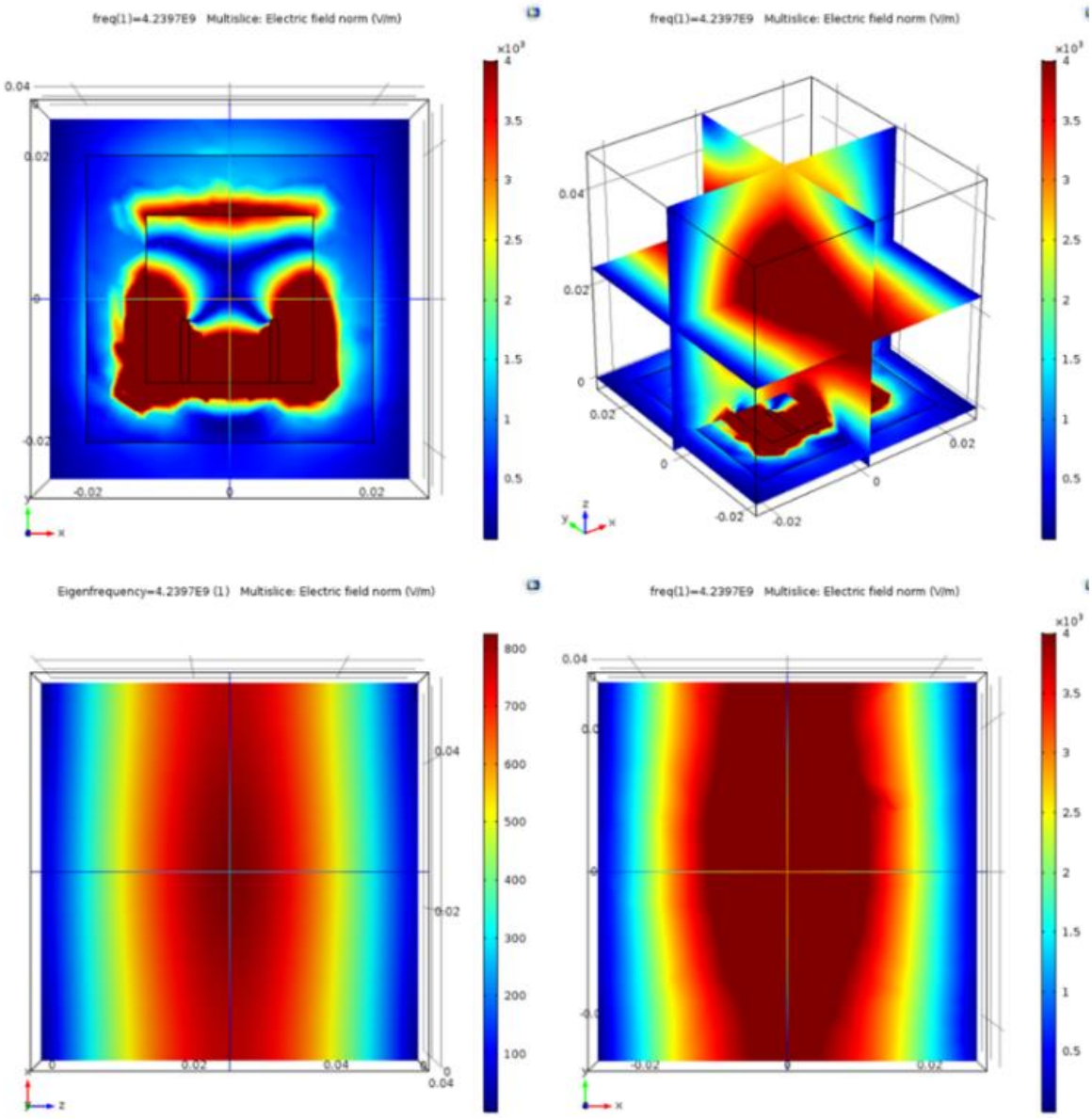

Figure 2.1.6 - a) A slice of the electric field at the antenna surface. b) A 3D view of the electric field in the rectangular cavity. c) X-Y plane of the analytical eigenmode electric field. d) X-Y plane of the electric field in the cavity driven by a micropatch antenna

It should be noted that the analytical solutions to resonant cavity modes can never be exactly replicated in the real-world due to many factors. These discontinuities are very apparent in Figures 2.1.5 and 2.1.6 a and b. These show that the micropatch antenna has fringing fields that are very high in magnitude when compared to the electric field of the resonant mode. It is

also visible in both figures that the magnitude of the electric field is much higher in the vicinity of the antenna and that these variances lead to a slight difference between the purely mathematical solution and the more realistic model. Despite the slight differences, modeling these cavities and antennas provided evidence that the COMSOL modeled micropatch antennas interacting with a conductive resonant cavity are able to produce the expected resonant mode.

2.2 Design of Resonant Cavity Models

The study carried out was a parametric design sweep of microwave resonant cavity geometries. These cavities were designed from a baseline of the conical frustum used in the NASA Eagleworks thrust test campaigns [33], [34]. The NASA Eagleworks frustum cavity is a truncated cone with a large diameter of 20.94 cm, a small diameter of 15.56 cm, and a height of 22.86 cm. The sizes of frustums that were studied were roughly ½ and ¼ the size of the full-sized NASA Eagleworks frustum. The larger cavity was designed to have a maximum dimension of 10 cm. This size constraint is due to the size of CubeSats, the most likely space based test bed for these devices [43]. The size constraint of 10 cm corresponds with the largest maximum dimension of a single unit CubeSat. Both the ½ and ¼ frustum designs were swept through an array of conic angles, from cylinder to a full cone, while retaining the same height and large diameter. The dimensions of all geometries that comprise the cavities that were investigated are displayed in Tables 2.2.1 and 2.2.2. Each frustum consists of a copper shell 1 mm thick, a micropatch antenna designed to emit at the cavity's resonant mode, and a HDPE disk. An example cutaway schematic of the resonant cavities is shown in Figure 2.2.1. These geometries were studied using the COMSOL RF and Thermophysics modules. Each individual component of the resonant cavities was designed using design equations from Pozar's Microwave Engineering and Stutzman's Antenna Theory and Design [44], [45]. Specifically the micropatch

antenna was designed using equations found in Antenna Theory and Design, Chapter Five, "Resonant Antennas: Wires and Patches" [45].

Table 2.2.1 - Dimensions of resonant cavities that were simulated.

	Larger Frustum Diameter [cm]	Smaller Frustum Diameter [cm]	Frustum Height [cm]	Copper Shell Thickness [mm]	Teflon Insert Thickness [cm]
1/2 Size Narrow Top Cavity	10	1.775	8.2	1.0	1.0
1/2 Size Scale Cavity	10	2.850	8.2	1.0	1.0
1/2 Size Wide Top Cavity	10	3.925	8.2	1.0	1.0
1/4 Size Narrow Top Cavity	5	0.8875	4.1	0.5	0.5
1/4 Size Scale Cavity	5	1.425	4.1	0.5	0.5
1/4 Size Wide Top Cavity	5	1.9625	4.1	0.5	0.5

Table 2.2.2 – Dimensions of resonant cavities that were simulated

	Eigenfrequency [GHz]	Micropatch H & W [cm]	Substrate H & W [cm]	Substrate Thickness [mm]	Feed Trace Width (tw) [cm]	Feed Inset Depth (x) [cm]	Inset Notch Width (y) [mm]	Antenna Bandwidth [% / dB]
1/2 Size Narrow Top Cavity	2.7734	3.57	4	2.54	1.13	1.35	1.80	1.31 / -18.83
1/2 Size Scale Cavity	2.7011	3.66	4	2.54	1.13	1.39	1.83	2.14 / -16.70
1/2 Size Wide Top Cavity	2.4711	4.00	4.5	2.54	1.13	1.52	2.00	1.17 / -19.32
1/4 Size Narrow Top Cavity	5.6499	1.75	2.5	2.54	1.13	0.66	0.8751	2.69 / -15.70
1/4 Size Scale Cavity	5.4114	1.83	3	2.54	1.13	0.69	0.9154	4.28 /-13.69
1/4 Size Wide Top Cavity	5.005	1.98	2.5	2.54	1.13	0.75	0.9878	2.37 / -16.25

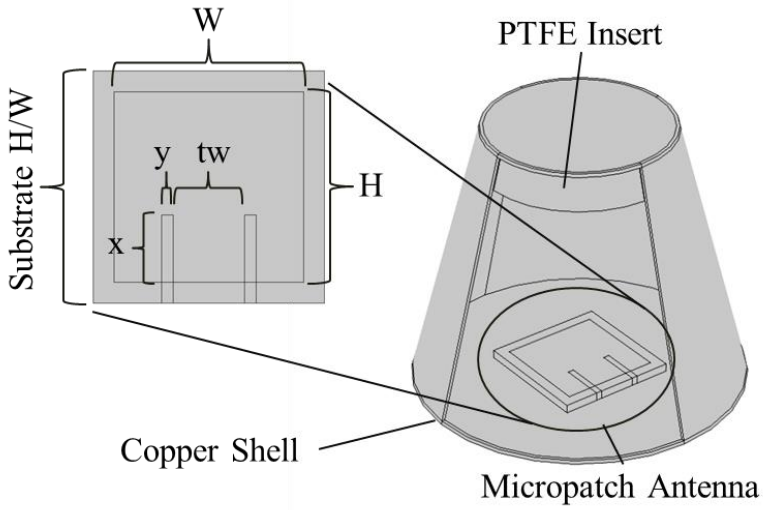

Figure 2.2.1 – Cutaway schematic of the resonant cavity and driving micropatch antenna with inset describing antenna dimensions.

The variables W and H are the width and height of the antenna. These dimensions were designed to be equal, creating a square micropatch antenna because the size of the cavity was a limiting design variable. As described in the background section, the width of the antenna controls the characteristic impedance. Making the width the same as the height raises the impedance and necessitates the use of an inset feed. The parameters for the inset feed are x, y, and tw. The inset feed depth, x, tunes the impedance of the micropatch antenna to match it to a 50 Ω network. The inset feed is given a trace width (tw) that also has a characteristic impedance of 50 Ω. The final design feature of the micropatch antenna's inset feed is the notch width, y. This width is 5% of the width of the antenna, a choice based on the paper published by Matin *et al.* [46].

The micropatch antenna design factors displayed in Figure 2.2.1 change for each cavity simulated. These factors are highly dependent on the frequency at which they were designed to operate. This frequency is at one of the resonant modes of the cavity that the antennas will be driving. Because the volume and other geometric values of the cavities are varied, six individual micropatch antennas had to be designed to match the eigenfrequencies of all six cavities. The necessity of knowing the eigenfrequencies of the cavities coupled with the fact that no analytical solution exists to the eigenmodes of a conical frustum required that a simpler model of the cavities be simulated in COMSOL. These simpler models were used only to find the eigenmodes and eigenfrequencies of the more complex models so that the driving antennas could be designed. These models consisted of the inner volume of the cavity described as a perfectly electrically conductive boundary with a dielectric Teflon insert shown in Figure 2.2.2.

One simple model was made for each more complicated Multiphysics model that was created later. They were simulated in COMSOL's RF module with the eigenfrequency study. As

well as finding the eigenfrequencies of the cavities to design micropatch antennas, the eigenfrequency study also gave an idealized view of what the resonant mode of the cavity should look like.

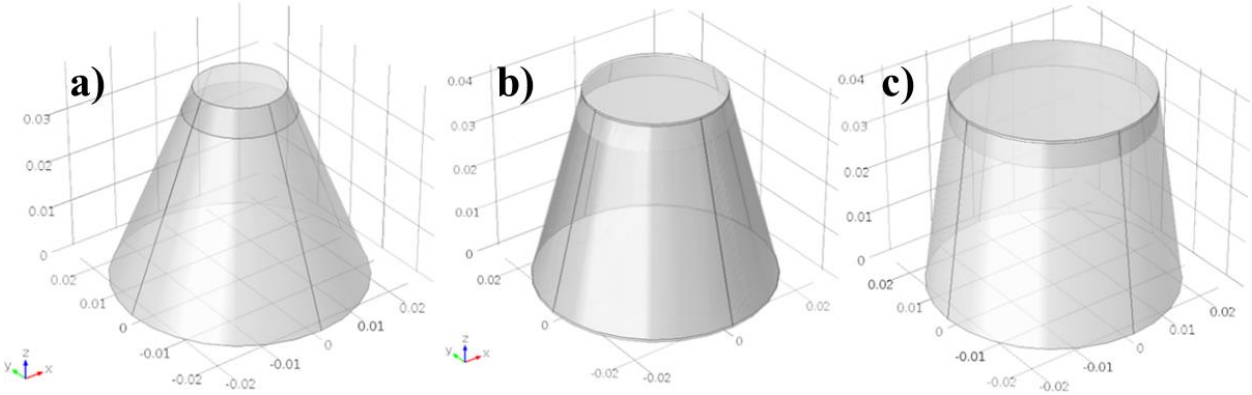

Figure 2.2.2 – Eigenmode test models: a) Narrow top 1/4 scale, b) 1/4 scale, and c) Wide top 1/4 scale.

Once the frequencies that the cavities would be operating at were known, the parameters were entered into design equations to create the antenna. The design equations were used in a Matlab script that automated the design procedure based on the input of a desired frequency, substrate material, substrate thickness, and copper trace thickness. This script can be found in Appendix B. The micropatch antennas were modeled as inset fed, single layer antennas with a substrate thickness of 0.1 in and a 35.56 μm copper thickness. The antennas were designed to work in a 50 Ω impedance system. A schematic of the micropatch antenna was shown earlier as an inset in Figure 2.2.1.

The design parameters of the micropatch antenna were the last values that had to be calculated before the final test models could be created and simulated. With the micropatch completed, the final Multiphysics model of the cavities was built. A schematic showing the ½ scale resonant cavity with its driving micropatch antenna was shown previously in Figure 2.2.1.

As seen in the figure, the micropatch antenna was located directly centered at the bottom of the large end of the frustum. Filling the small end of the cavity to a depth described in Table 2.2.1 was the Teflon insert.

2.3 COMSOL Computational Model Settings

All six cavities that were investigated were simulated using the COMSOL RF and Heat Transfer modules. Combined, the COMSOL RF and Heat Transfer modules simulate microwave heating, while independently, the EM module simulates all electromagnetic aspects of the cavity. The Microwave Heating Multiphysics module models all electromagnetic losses as heat sources for the Heat Transfer module. The Heat Transfer module models the heat transfer from input heat sources through all heat transfer modes, conduction, convection, and radiation. The Heat Transfer module also allows the pressure of any fluid media to be set.

2.3.1 Materials

The cavity model shown in Figure 2.2.1 was made of three different materials, all materials come preinstalled in COMSOL's materials library. The exterior shell of the cavity and the patch antenna are composed of copper. The material properties that were used in this simulation are shown in Table 2.3.1.1.

Table 2.3.1.1 - Material properties of copper used in the simulations.

Copper	
Electrical Conductivity	5.998e7 [S/m]
Relative Permittivity	1
Density	8960 [kg/m^3]
Heat Capacity	385 [J/(kg*K)]
Thermal Conductivity	400 [W/(m*K)]

The material of the micropatch antenna substrate as well as the dielectric insert are composed of high density polytetrafluoroethylene (HDPTFE), most commonly known by its trade name, Teflon. HDPTFE was chosen as a dielectric material because of its use in the cavities that were investigated by TU Dresden and NASA Eagleworks. Teflon was chosen in the other experiments for its beneficial dielectric characteristics, namely its high resistivity and breakdown voltage. The material properties of HDPTFE that were used in the simulations is displayed in Table 2.3.1.2.

Table 2.3.1.2 - Material properties of HDPTFE used in the simulations.

HDPTFE	
Electrical Conductivity	10e-24 [S/m]
Relative Permittivity	2
Relative Permeability	1
Loss Tangent	0.00022 [rad]
Density	2200 [kg/m3]
Heat Capacity	1050 [J/(kg*K)]
Thermal Conductivity	0.24 [W/(m*K)]

The final material used in the cavity was air. Air was used as the material that occupied the interior of the cavity. As mentioned previously, the pressure of any fluid material can be set through the Heat Transfer module. Because the cavities will be tested in vacuum, the pressure of the air inside the cavity was set to 1 Pa (7.5 mTorr). This pressure is similar to a rough vacuum that could be generated in vacuum chambers incapable of generating extremely low pressures. For both the electrical and thermal portions of the simulation, the air material can be considered to simulate vacuum. Table 2.3.1.3 shows the electrical properties of the air material.

In addition to the three electrical properties listed in Table 2.3.1.3, COMSOL also used gas laws to calculate the heat capacity at constant pressure, the density, and the thermal

conductivity of the material. These properties were updated in time according to the gas law for air for changing pressure and temperature. The units for these properties can be seen in the tables that describe the equivalent property for the other units used in the cavities.

Table 2.3.1.3 - Material properties of air used in the simulations.

Air	
Electrical Conductivity	0 [S/m]
Relative Permittivity	1
Relative Permeability	1

2.3.2 Boundary Conditions and Physics Settings

COMSOL also requires that the physics modules being used have clear definitions of all boundary conditions and characteristic equations for all boundaries and domains within the model. In COMSOL, a domain is a volume bounded by known conditions. The volumes describe the resonant cavity model. These selections help limit and define the simulation to match the physics that are required to recreate the real-world model of a resonant cavity and micropatch antenna. Descriptions of the settings used for the RF, Heat Transfer, and Microwave Heating modules are necessary to duplicate the model. Because the resonant cavities are RF devices, the RF module physics required the most “instruction” before it accurately represented a physical resonant cavity. Even with the COMSOL resonant cavities modeled in a complex manner, there are still simplifications that were necessary due to computational limitations. Specifically, surface roughness wasn’t considered and the conducting boundaries of the micropatch antenna had to be modeled as perfect electric conductors. These allowances and their effects on the results will be discussed in depth in the Results and Discussion chapter.

The RF module required the most alteration to model the resonant cavities and driving antennas. The module describes the electromagnetic field model of a domain based on the

equation that most accurately represents the electric displacement field model of the material. This setting is known as the Wave Equation domain setting. The cavity resonator model required that the material domains be split up into two different Wave Equation settings. The first Wave Equation setting is based on the relative permittivity of the material and modeled the electromagnetic field in the copper and air material domains. The other Wave Equation setting was used on the HDPTFE material domains. This Wave Equation setting modeled the electric displacement field based on the loss tangent of the material. Together, these two wave equations modeled the electromagnetic field in all domains of the resonant cavity.

Initially, all boundaries in the RF module are modeled as perfect electric conducting boundaries. To model a realistic conductor with losses, the boundary condition setting "Impedance Boundary Condition" must be applied. This boundary condition was applied to all copper material boundaries. This boundary condition is also necessary for the Multiphysics aspect of the simulation. The losses due to the surface impedance from induced surface currents are input as a heat source for the Heat Transfer module. A significant exception that had to be made were the boundary conditions on the micropatch antenna.

The micropatch antenna COMSOL model required that both the micropatch and the ground plane be perfectly electrically conductive boundaries. This means that the simulation will compute no electrical losses on the conducting surfaces of the antenna and therefore no heating due to losses on these surfaces. This is due to the requirements of the Lumped Port boundary condition. The Lumped Port boundary condition is the boundary that drives the antenna and has settings that define input power, frequency, and system impedance. All antennas were designed around a 50 Ω impedance system. The frequencies used for each cavity were given in Table 2.2.2. The input powers used were 100 W rms for the ¼ scale cavities and 400 W rms for the ½

scale cavities, corresponding to an input voltage of 100 V and 200 V, respectively. This was because the ½ scale models had volumes four times the size of the ¼ scale models and it was desired to keep the power to volume ratio the same. The Lumped Port boundary condition simulates the appearance of the antenna being part of a larger network balanced to the system impedance setting. For all simulations, the initial electromagnetic values were set to zero.

The Heat Transfer module is much simpler to set up to accurately simulate the heat transfer model of the resonant cavity. When working with the heat transfer module alone, heat sources must be added independently to track the transient heat transfer model of whatever geometry you are testing. However, the use of the COMSOL Multiphysics module models the electric losses (both volume and surface losses) set up in the RF module as the heat sources for the material. These heat sources are then used as the input power portions of heat transfer equations of the simulated device. The settings that govern the heat transfer model of the resonant cavity were the Heat Transfer in Solids domain setting, the Thermal Insulation boundary setting, the Boundary Heat Source boundary setting, and the Heat Source domain setting.

Enabling the Heat Transfer in Solids domain setting allows for COMSOL to model heat transfer through that domain. Removing a domain from this module can be thought of as completely thermally isolating a volume. Because it was desired to model the heat transfer of the entire cavity, all domains were included in this setting. The domain making up the interior volume of cavity was modeled as air at 1 Pa. The density of the air material is dependent on its pressure. Due to the low pressure of the air, it's thermal conductivity was very low. Therefore, the heat transfer of the resonant cavity can be thought of as almost entirely confined to the solid components of the system, the cavity, the antenna, and the HDPTFE insert. At the intersection

between two different materials, there exists a contact thermal resistance. This thermal resistance is modeled by the Thermal Insulation boundary condition, all boundaries were included in this setting.

The energy input for the Heat Transfer module is from the RF losses due to the power injected from the Lumped Port boundary setting. To include these losses into the heat transfer model, the Boundary Heat Source boundary condition and the Heat Source domain condition must be added. The Heat Source domain setting was used on the domains that were composed of HDPTFE. This is because the losses in a dielectric occur in the volume of the material. The Boundary Heat Source condition was applied to all copper boundaries. Due to the skin effect, the electric losses of conductive metals are modeled on the surface of the conductor which means the heating from those losses is modeled on the boundary of the conductor. For all domains, the initial temperature was set to 293.15 K [44], [47]–[49].

These settings fully describe the EM and Heat Transfer portions of the resonant cavity model in COMSOL. However, for the RF and Heat Transfer modules to interact, a Multiphysics module must be added. The interaction between these modules is defined by the Microwave Heating module. The Microwave Heating Multiphysics module introduces the link allowing the RF losses to be used as a heat source through two settings: The Microwave Heat Source domain condition, and the Boundary Microwave Heat Source boundary condition. Both the domain and boundary microwave heat source settings allow the losses in the EM model to be used as power input sources for the heat source setting in the Heat Transfer module.

2.3.3 Meshing and Solver Settings

COMSOL completes the finite element analysis computations of the RF and Heat Transfer system by breaking the model down into a tetrahedral mesh. The mesh generates volumes within the resonant cavity geometries that are used as the individual elements at which the simulation equations are calculated. The computational model arrives at a solution by checking the solution boundary conditions of the tetrahedral mesh. The quality of the solution output by the computation is highly dependent on the mesh settings that are used. The mesh setting that has the most effect on the solution is the size of the mesh. The maximum size for the mesh defines the minimum size of 3D features that can be computed. By decreasing the volume of the individual mesh tetrahedrons and increasing their density and number, the accuracy of the solution is increased. When mesh sizes are too large, the error accumulates across their volume. This causes individual tetrahedron solutions to converge to incorrect values.

The meshes used in the six resonant cavities had settings based on the physics modules used. Because the RF module was used, the minimum mesh element size was set based on a fraction of the wavelength of the EM wave. For all simulations ran, the maximum mesh size was set at 20% the wavelength used. COMSOL used several different solver methods to run the computations. The number of tetrahedral mesh elements ranged between roughly 300,000 for the smallest cavity, to 750,000 for the largest cavity. This corresponded to a range of roughly 1.5 – 4 million degrees of freedom that had to be solved for. For all eigenvalue problems, the solver method used was the MUltifrontal Massively Parallel sparse direct Solver (MUMPS). The Multiphysics simulations were set to use two solvers: the Biconjugate Gradient Stabilized method (BiCGStab) and Generalized Minimal Residual Method (GMRES).

2.3.4 COMSOL Study Selections and Descriptions

Multiple COMSOL studies were used in the completion of the simulations of the resonant cavities. For the simplified cavities used to find the eigenfrequencies and eigenmodes of the cavities, the preinstalled COMSOL Eigenfrequency study was used. This study is set up in the frequency domain of the resonant cavity. Using the physics described earlier in the Background section, the solver will find eigenfrequencies and eigenmodes around a frequency that is set in the studies. If a value is not set in the eigenfrequency solver, the solver will default to searching for eigenmodes around 0 Hz. When working on cavities that have modes in the GHz range, this can result in finding non-physical solutions that meet the solution requirements for the solver. These solutions are easy to spot because they do not have well developed mode shape like physical solutions and almost always have a significant imaginary portion to their frequency. Due to these results, it is a good idea to have a range at which you expect the eigenfrequencies of whatever system you're working on and to search for eigenfrequencies in this range.

The other study that was used was the "Frequency-Transient study." This was the study that was used in the Multiphysics simulations of the resonant cavities. It is purpose built for studying the phenomena of microwave heating. The name implies how the study works. The study solves the electromagnetic portion of the simulation in the frequency domain independently at each time step. The EM values that are used in the Heat Transfer module are then input from the frequency domain solution into the transient heat transfer portion of the study. The transient effects of the heat transfer module are then fed back into the next frequency domain solution. This continues for each time step calculated. Each individual time step has a frequency domain solution that is solved independently from the previous frequency domain solution. This process continues for the entire computation time. The Frequency-Transient study

has a built-in setting that determines the time steps and time of the full simulation. Just like the mesh setting is more accurate the denser the mesh, the transient portion of the study is more accurate the denser the time steps are. All simulations ran at a time step of 0.1 s; the ½ scale models ran for 250 s and the ¼ scale models ran for 100 s. The time required to run these solutions varied from roughly 30 minutes for the smallest cavity, to just over an hour for the largest cavity.

2.3.5 Plotting and Evaluations Tools

Once the solutions were completed, there were a wide range of plotting tools and analyses available based on the data output by the study. These include 3D plots, surface plots, slices, and all forms of integration. These tools can be used on all data sets available from the study. For a full list of all data sets that the Microwave Heating module outputs, the COMSOL 5.2 User's Guide may be consulted [42]. For the purpose of compiling and presenting relevant data, several plots were used and several integrations of the data sets were performed. The plots that were created for each cavity were a multislice of the EM field intensity, a surface plot of temperature, a surface plot of surface resistive losses, and a surface plot of volume resistive losses. In addition, several integrals were performed in order to calculate the Quality Factor of the cavity.

The EM field inside the cavity was plotted as a multislice. This plotting form projected xy, xz, and yz planes onto the model. It is possible to control the number and location of these planes as well as to change their data range. The appearance of the plots can also be chosen, the setting chosen for the appearance of the multislices plotted was COMSOL's "rainbow" setting. This setting visually represents the range of data as colors from blue (lowest values) to dark red (highest values). By plotting the data as multislices, it was possible to get a good view of the 3D

shape of the electric field while also being able to view the electric field intensity on 2D surfaces like the top plane of the micropatch antenna.

The temperature of the cavity was plotted as a surface plot. The surfaces plotted are all surfaces of the 3D model of the cavity. Because all surfaces are plotted, it was necessary to hide domains in order to get an interior view of the cavity so that the temperature of the Teflon insert and the micropatch antenna could be seen. For all temperature plots, the color range setting "spectrum" was used. This setting is similar to the "rainbow" setting used for the EM field intensity slices, but instead of using the color blue for the low data ranges, the "spectrum" setting uses violet. Also different is that the "spectrum" setting has distinct color steps for intermediate ranges of data within the full dataset, while the "rainbow" setting smoothly develops from one color to the next. These distinct steps in the data make it easier to interpret the temperature range throughout the resonant cavities.

Surface plots were also used to visualize the RF losses that happened in the cavity, because the loss regime for each type of material domain was different, both surface resistive losses and dielectric losses were plotted in the same surface plot. The surface resistive losses are confined to the portions of the cavity that are made out of copper and the dielectric losses are limited to the part of the cavity that are Teflon. Like the temperature surface plots, the "spectrum" color range setting was also used to plot the losses.

In addition to the visual plots, several integrals of data included in the study output were conducted in order to find the Quality Factor. Integrals in COMSOL are extremely simple to implement, under component couplings in the local definitions portion of the geometry creation window there is an option to add integrals to the computation. After adding the integral, its

settings can be changed to be confined to a certain region of the model or include the entire model. This setting window also allows you to control the name of the integral operator, what region the integral will be integrating, and if the integral is a volume, surface, time, or other kind of integral. To find the Quality Factor, it was necessary to create three separate integral operators.

These integral operators were used to find the total energy contained in the electric field of the cavity, the resistive surface losses of the cavity, and the resistive volume losses of the cavity. These three values are necessary to find the Quality Factor of a resonant cavity.

$$Q = 2\pi f * \left(\frac{Energy\ in\ Electric\ Field}{Surface\ Losses + Volume\ Losses}\right) \qquad \text{(Equation 2.3.5.1)}$$

The variable Q is the Quality Factor, and f is the resonant frequency of the cavity. If the reader is familiar with the physics defining resonant cavities, they would note that there is an extra term contained in this calculation for Quality Factor. Most definitions in textbooks do not include volume resistive losses in their consideration of the Quality Factor. This is because most resonant cavities do not have components within them and all losses are due to the surface losses of the conductive walls of the cavity. Because the resonant cavities that were part of these studies had internal features made from Teflon, volume resistive losses had to be considered in the calculation of Quality Factor.

The integrals created at this point have no integrand and can be thought of as only an integral operator. To create an integrand and get a result, a variable must be created that is the result of the integration. For the simulations that were ran, these are the variable names that were used:

$$EzEn = int\_v(emw.Wav) \quad \text{(Equation 2.3.5.2)}$$

$$surfl = int\_s(emw.Qsh) \quad \text{(Equation 2.3.5.3)}$$

$$resl = int\_v2(emw.Qrh) \quad \text{(Equation 2.3.5.4)}$$

$EzEn$ was the name given to represent the energy contained in the electric field, $surfl$ was the variable name given to the resistive surface losses, and $resl$ was the variable name given to the volume resistive losses. The integral operators int_v and int_v2 were volume integrals and the integral operator int_s was a surface integral. All volume integrals integrated over the entire volume of the resonant cavity, and the surface integral integrated over all surfaces of the cavity. The integrands that the integrals are operating on are internal variable names contained in COMSOL's data output. The prefix "$emw.$" denotes that the data set being operated on is from the RF electromagnetic wave dataset. The variable $emw.Wav$ is the average electric field intensity, $emw.Qsh$ represents the resistive surface losses, and $emw.Qrh$ represents the resistive volume losses. In order for these data to be output at the end of a computation, a "global evaluation" must be made for each variable that is desired to be output. The global evaluation instructs COMSOL to display the data requested in a tabular form. All four of these variables were output as global evaluations at the end of the computation: $Q, EzEz, surfl, resl$.

Chapter 3: Results and Discussion

For the six cavities that were simulated, three plots were created from the dataset that was output: an EM multislice with one slice each in the yz and zx planes, and two slices in the xy plane; a surface plot showing the temperature of the resonant cavity; and, a surface plot showing the induced RF losses. In addition, six simplified cavities were modeled in order to study the eigenfrequency and eigenmodes of the cavities in order to design the micropatch antennas that were used.

Using a simplified resonant cavity model described in the Experimental Method section, the eigenfrequency of the cavities was found. Figures 3.1, 3.2, and 3.3 show EM multislices of these cavities for the ½ scale model resonant cavities. The eigenfrequency for the ½ scale model was 2.7011 GHz. The ½ scale wide top model had an eigenfrequency of 2.5022 GHz and the ½ scale narrow top model had an eigenfrequency of 2.8188 GHz.

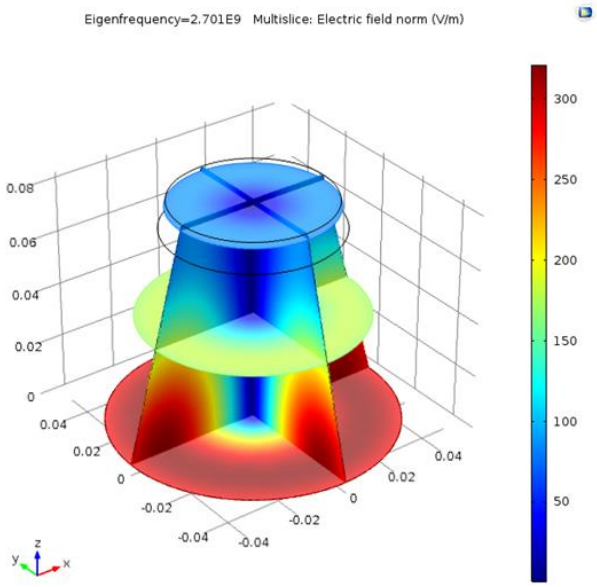

Figure 3.1 - EM Multislice and eigenfrequency of the 1/2 scale model resonant cavity model.

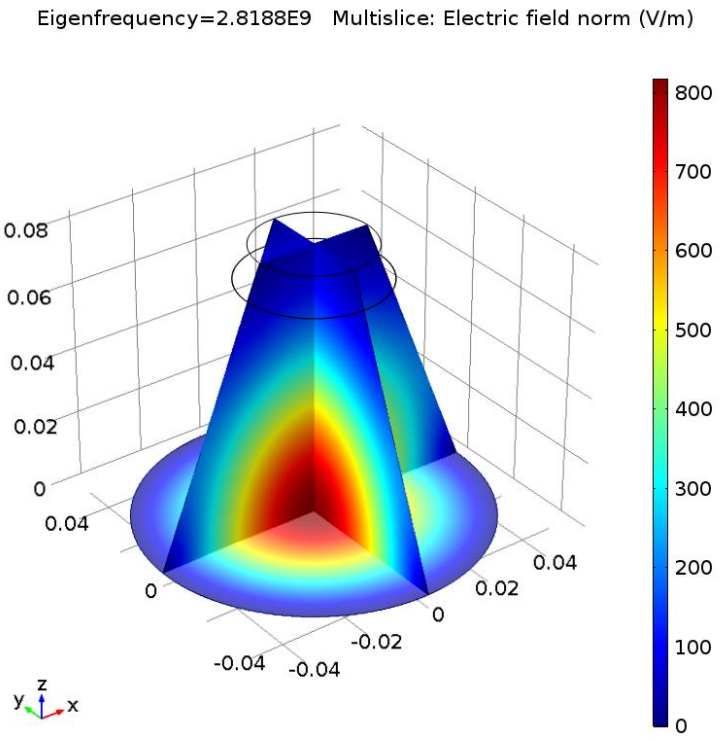

Figure 3.2 - EM Multislice and eigenfrequency of the 1/2 scale narrow top resonant cavity model.

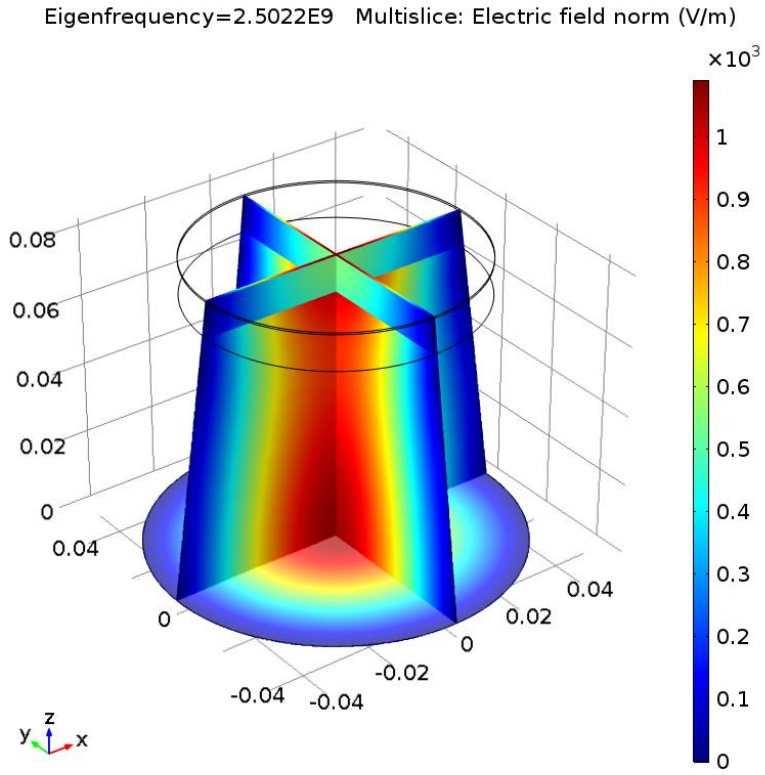

Figure 3.3 - EM Multislice and eigenfrequency of the 1/2 scale wide top resonant cavity model.

It is noteworthy that the mode shape of the electric field for the ½ scale model is a nonphysical computational solution. The correct physical mode is more similar to the field seen in Figure 3.2 in the narrow top model. The physical mode can also be seen represented in the Multiphysics ½ scale model that will be discussed later in the Results chapter.

The eigenfrequencies for the ¼ scale models were found in the same manner. The eigenfrequency for the ¼ scale model was found to be 5.4114 GHz, the eigenfrequency for the ¼ scale narrow top model was 5.634 GHz, and the eigenfrequency found for the ¼ scale wide top model was 5.003 GHz. The figures that display the EM multislices and eigenfrequencies are Figures 3.4, 3.5, and 3.6.

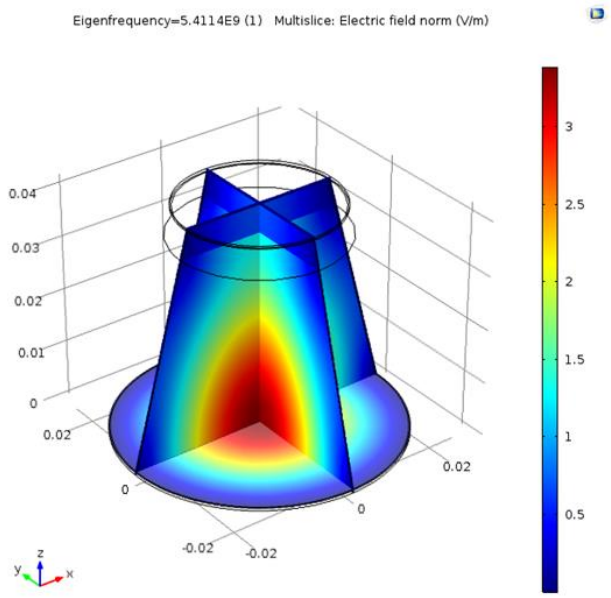

Figure 3.4 - EM Multislice and eigenfrequency of the 1/4 scale resonant cavity model.

These eigenfrequency models were then used to design the micropatch antennas to drive the resonant cavity models described in the Experimental Methods chapter. For each cavity, simulated electric field multislices were taken to study the field patterns in the cavity and on the

micropatch antenna. The ½ scale model electric field slice diagrams can be seen in Figures 3.7, 3.8, and 3.9.

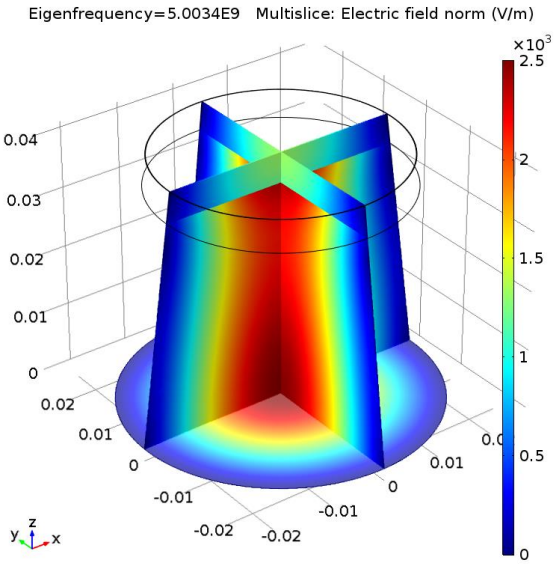

Figure 3.5 - EM Multislice and eigenfrequency of a 1/4 scale wide top resonant cavity.

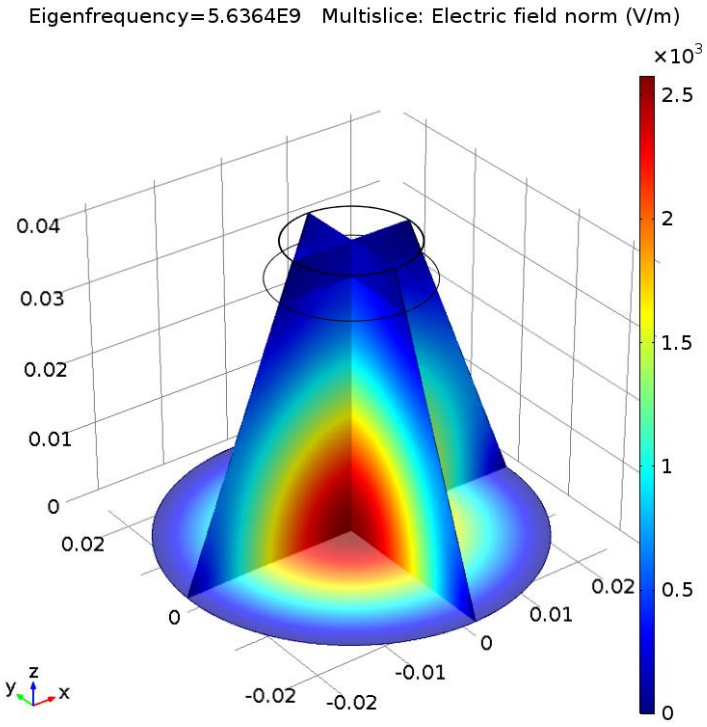

Figure 3.6 - EM Multislice and eigenfrequency of a 1/4 scale narrow top resonant cavity.

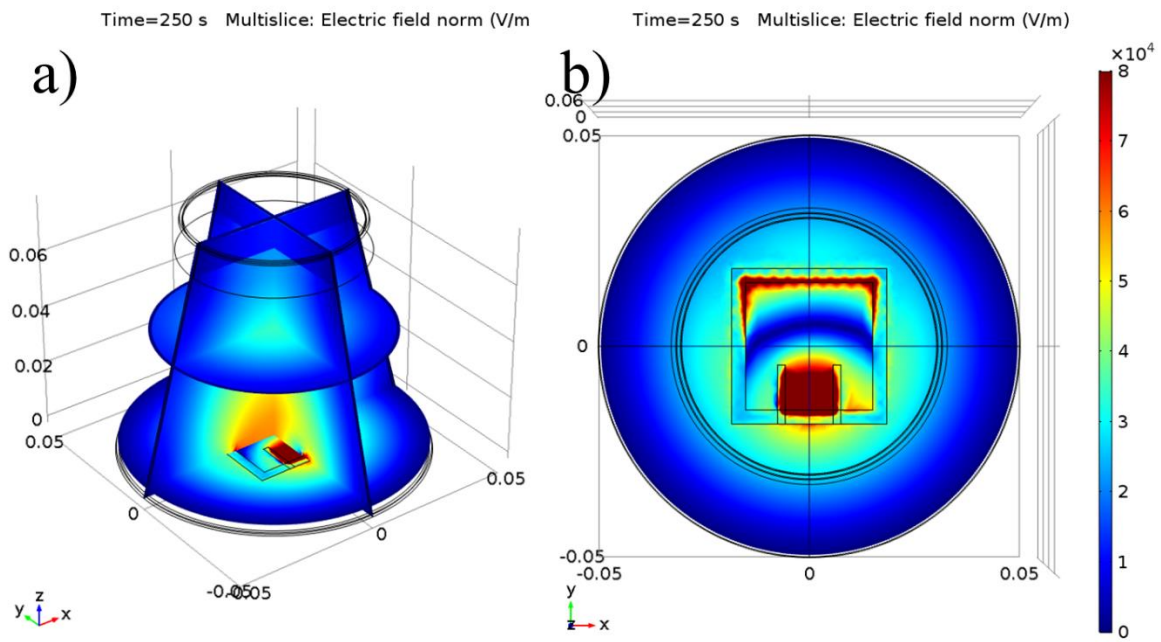

Figure 3.7 - Multislice of the electric field magnitude for a 1/2 scale resonant cavity model: a) a 3D view of the electric field shape within the cavity, b) the electric field on the surface of the micropatch antenna.

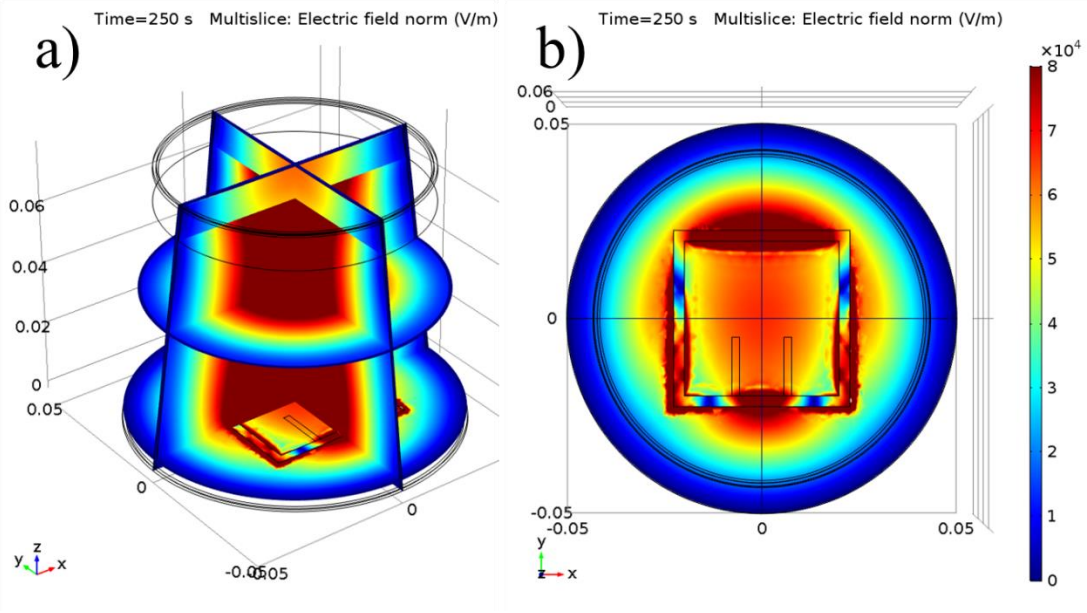

Figure 3.8 - Multislice of the electric field magnitude for a 1/2 scale wide top resonant cavity model: a) a 3D view of the electric field shape within the cavity, b) the electric field on the surface of the micropatch antenna.

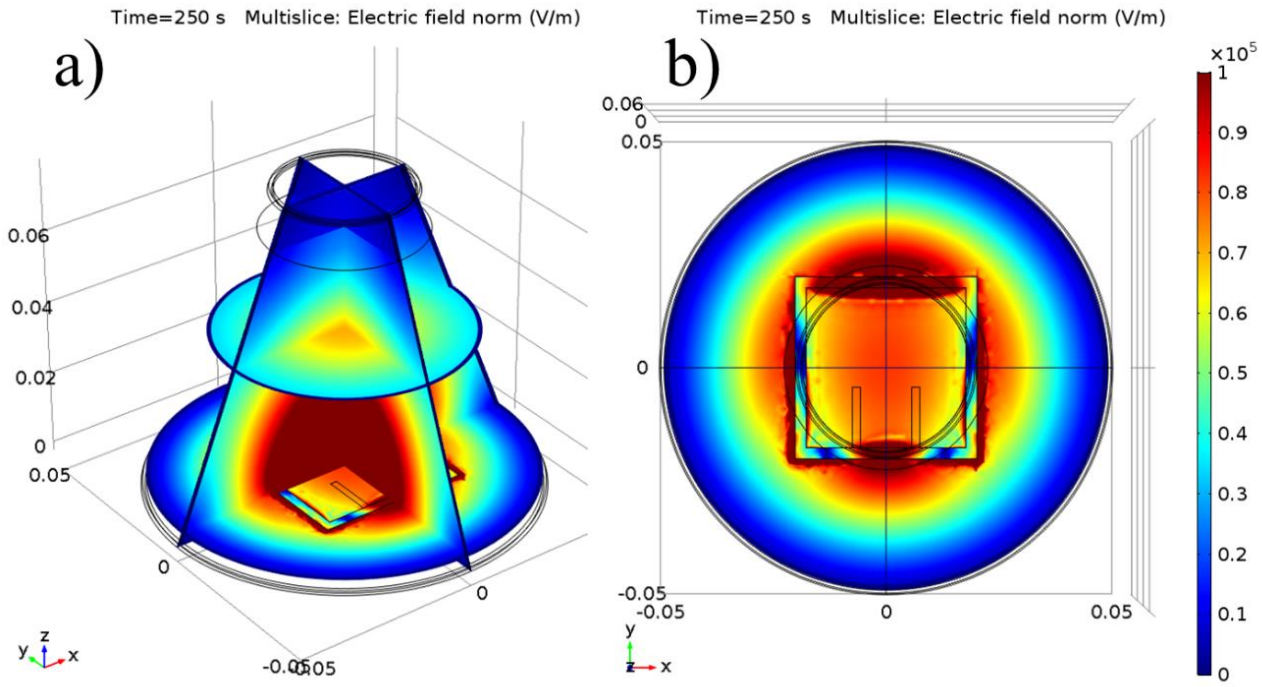

Figure 3.9 - Multislice of the electric field magnitude for a 1/2 scale narrow top resonant cavity model: a) a 3D view of the electric field shape within the cavity, b) the electric field on the surface of the micropatch antenna.

The resonant cavities each had similar maximum electric field intensities. The ½ scale model had a maximum field intensity in the cavity of approximately $6 * 10^4$ V/m, with intensities on the micropatch antenna reaching $8 * 10^4$ V/m. The ½ scale wide and narrow top cavities were computed to have maximum field intensities of 10^5 V/m. A noticeable effect of the presence of a dielectric insert can be seen in all three figures. The Teflon insert at the top of all cavities noticeably reduces the magnitude of the electric field on its interior. Also present in all three micropatch antennas are noticeable fields between the patch and the grounding plane. This problem can be remedied in future iterations of this antenna design by expanding the dimensions of the substrate. Fringing fields impede the antennas operation as a half-wave resonator by interfering with the field oriented in directions beneficial to the action of the antenna [45].

A consideration that must be made with micropatch antennas simulated in COMSOL is that the ground plane and patch of the antenna must be modeled as perfect electric conductors. If the same antennas were created, they would be less efficient due to losses in the copper trace.

The same electric field magnitude multislice plots were recorded for the ¼ scale models. These plots can be seen in Figures 3.10, 3.11, and 3.12. The electric field densities of all three cavities reached 10^5 V/m, both on the surface of the antenna and in the cavity. The field shapes of the cavities are highly analogous to the fields seen in the eigenfrequency studies. A noted difference between the ¼ scale models and the ½ scale models is that in the ¼ scale models, the fringing fields are much more highly contained to the micropatch antenna. A notable feature of the electric field density plots is where the field density is highest, these locations in the antenna and Teflon insert are the locations of the highest temperature.

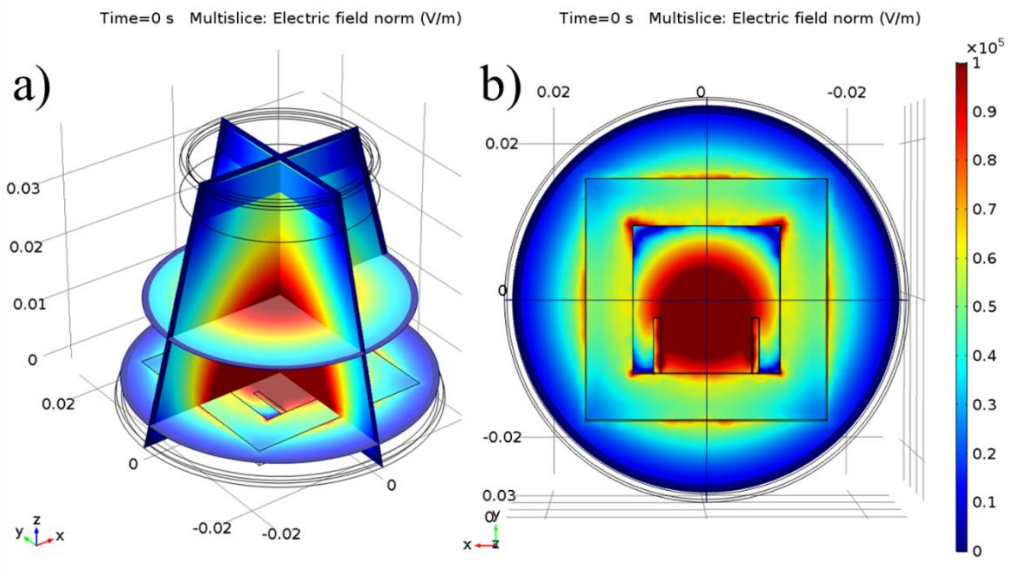

Figure 3.10 - Multislice of the electric field magnitude for a 1/4 scale resonant cavity model: a) a 3D view of the electric field shape within the cavity, b) the electric field on the surface of the micropatch antenna.

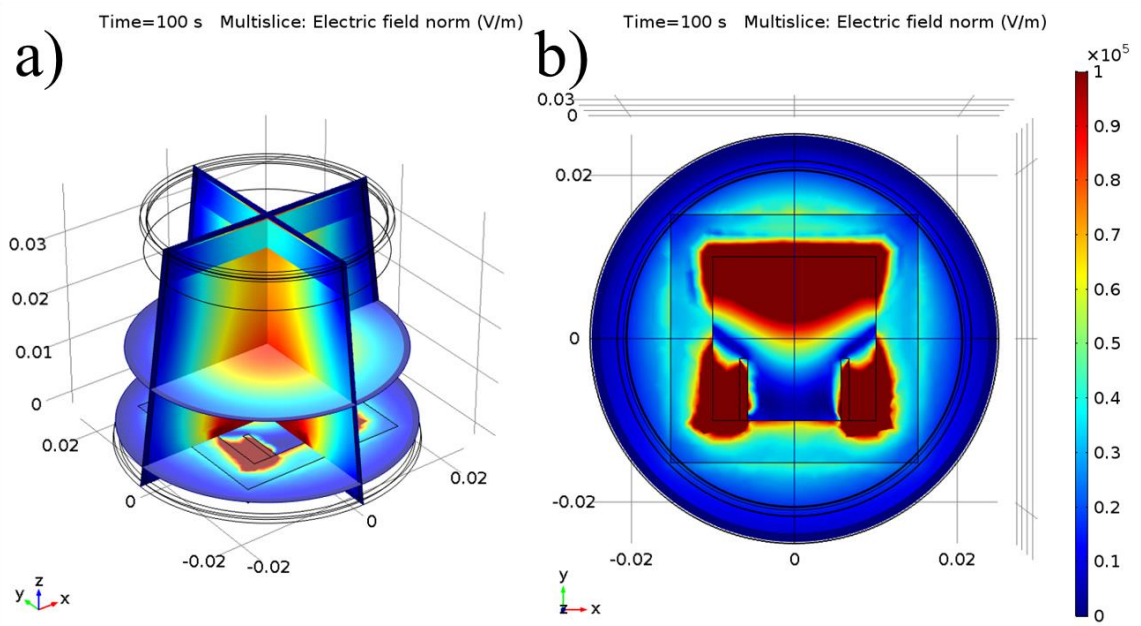

Figure 3.11 - Multislice of the electric field magnitude for a 1/4 scale wide top resonant cavity model: a) a 3D view of the electric field shape within the cavity, b) the electric field on the surface of the micropatch antenna.

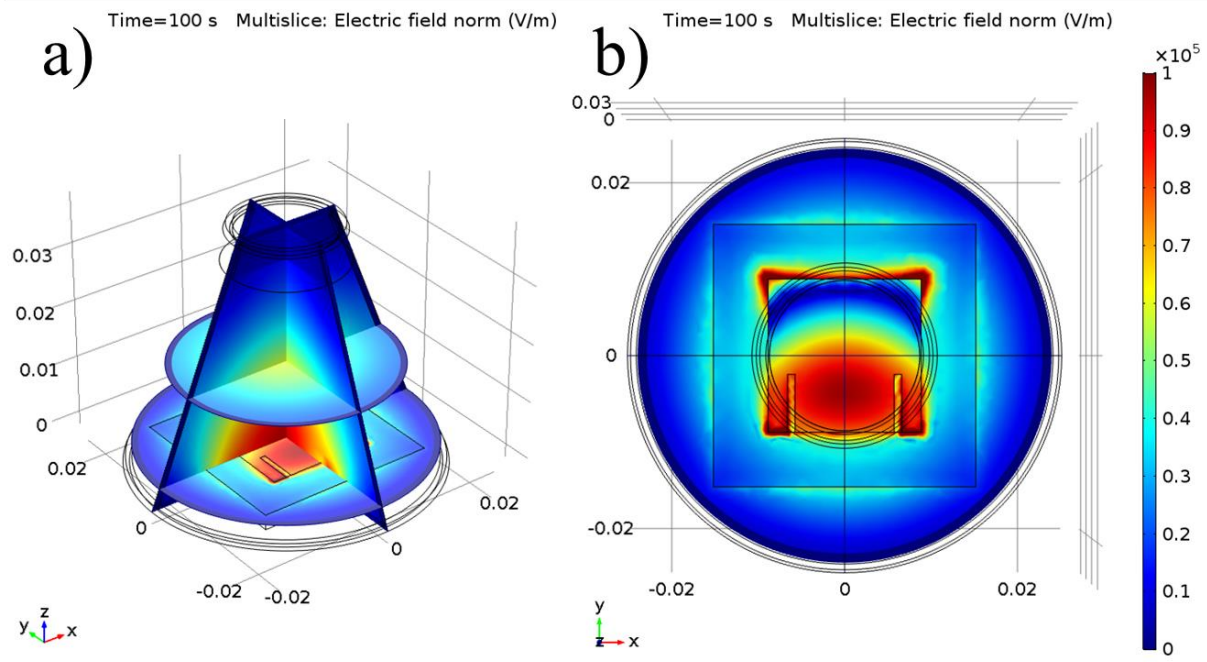

Figure 3.12 - Multislice of the electric field magnitude for a 1/4 scale resonant cavity model: a) a 3D view of the electric field shape within the cavity, b) the electric field on the surface of the micropatch antenna.

The electric field densities of all three cavities reached 10^5 V/m, both on the surface of the antenna and in the cavity. The field shapes of the cavities are highly analogous to the fields seen in the eigenfrequency studies. A noted difference between the ¼ scale models and the ½ scale models is that in the ¼ scale models, the fringing fields are much more highly contained to the micropatch antenna. A notable feature of the electric field density plots is where the field density is highest, these locations in the antenna and Teflon insert are the locations of the highest temperature.

The temperature data were presented as 3D surface plots. These are presented for the ½ scale models in Figures 3.13, 3.14, and 3.15. The copper body of the cavity can be seen to have a nearly homogenous temperature, while the components made of Teflon have concentrated warm spots. This is due to the thermal conductivity of the material. Copper has a very high thermal conductivity, so all thermal input spreads evenly throughout the volume. Teflon has a much lower thermal conductivity, so heat tends to "build up" in an area before it can be transmitted to surrounding areas. The initial temperature of all components in the cavity was set to 293.15 K at a time of 0 s. The ½ scale resonant cavity models were simulated for 250 s.

As noted in the discussion of the of the electric field plots, the temperature is seen to be highest in the locations that also have the highest electric field magnitude. The heating due to microwave losses is most severe in the antenna. In all ½ scale resonant cavity model antennas, portions of the antenna heated up at least 12 K. This is roughly equivalent to a rise from 68° F to 90° F. The copper skin of the cavity also rose uniformly in temperature from 293.15 K to ~295 K for the ½ scale model, ~297 K for the ½ scale wide top model, and ~296 K for the ½ scale narrow top model. There are also concentrations of heat located on the side of the Teflon insert facing the micropatch antenna. This effect is more subdued in the ½ scale model and the ½ scale

narrow top model as the electric field in these is more confined to a “bullet” shape. However, in the ½ scale wide top model, the field mode more closely resembles a cylinder. Due to this, the field intensity next to the cylinder is higher in the wide top model than in the other two models. This led to the increase in temperature much higher in magnitude than the other two cylinders. While the Teflon inserts in the ½ scale model and the ½ scale narrow top model only saw a temperature rise of approximately 2 K, the insert in the ½ scale wide top model rose 12 K to a temperature of 305 K.

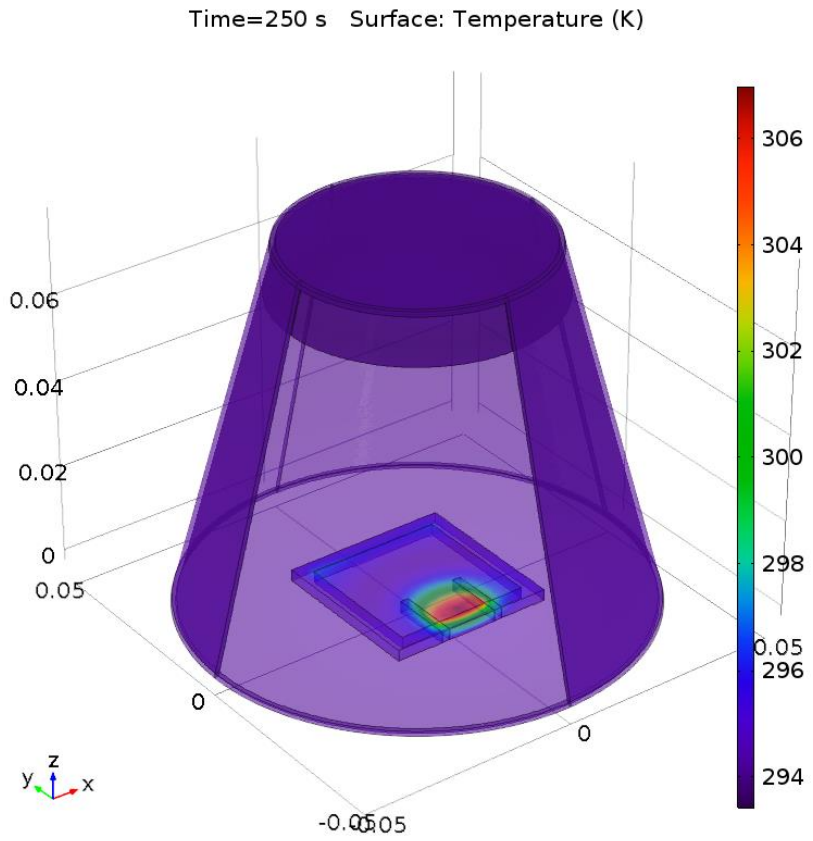

Figure 3.13 - Surface temperature plot for a 1/2 scale resonant cavity model.

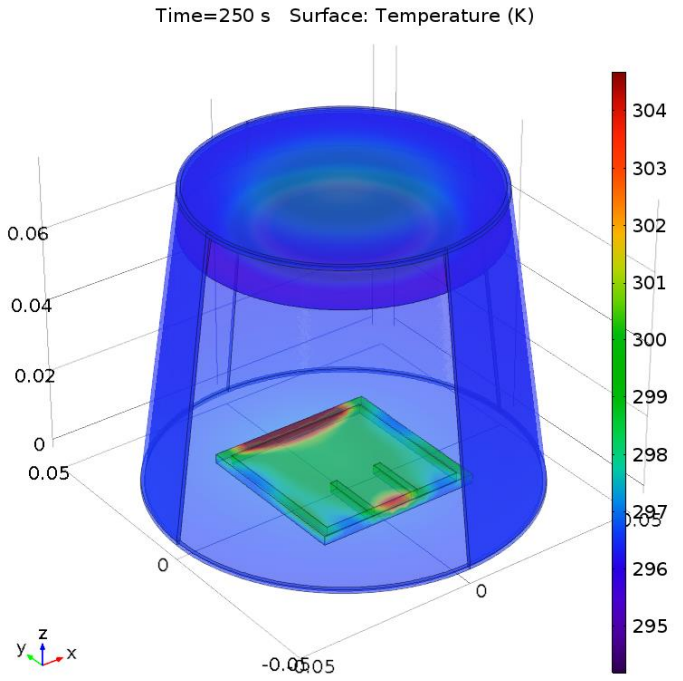

Figure 3.14 - Surface temperature plot for a 1/2 scale wide top resonant cavity model.

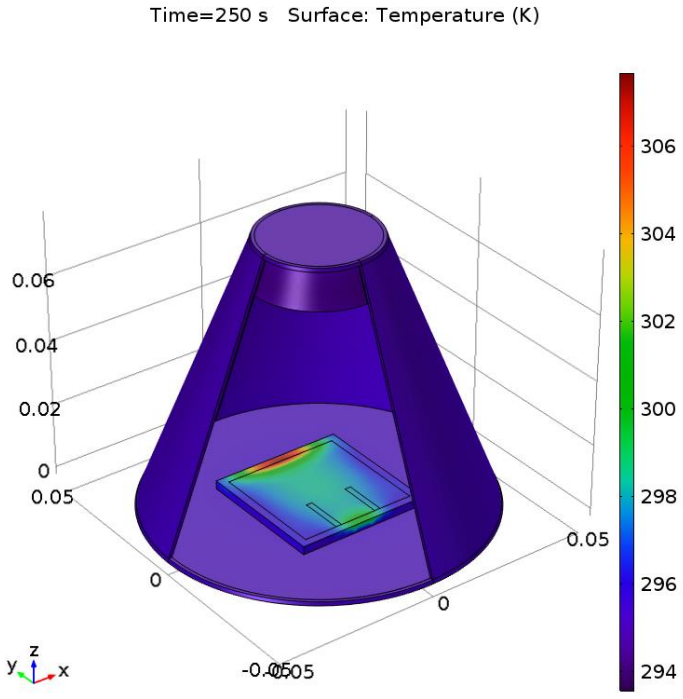

Figure 3.15 - Surface temperature plot for a 1/2 scale narrow top resonant cavity model.

Temperature plots for the ¼ scale resonant cavity models were also prepared. These plots are shown in Figures 3.16, 3.17, and 3.18. The ¼ scale resonant cavity models were simulated for 100 s. A segment of the copper cavity wall is hidden to directly show the micropatch antenna.

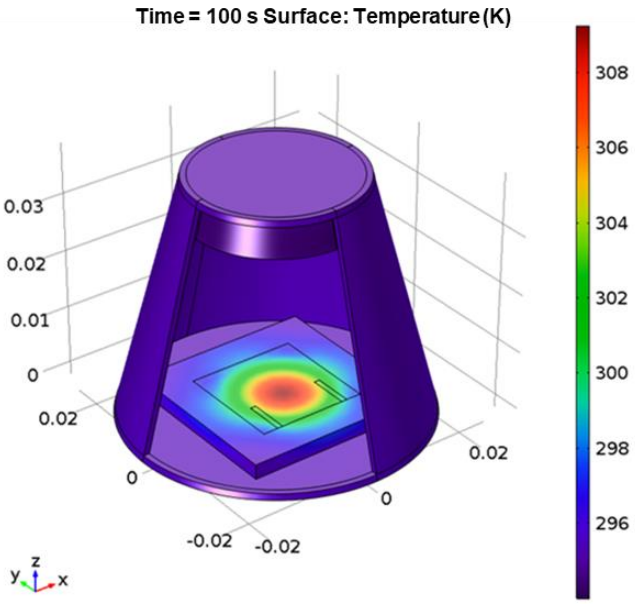

Figure 3.16 - Temperature plots of a 1/4 scale resonant cavity model.

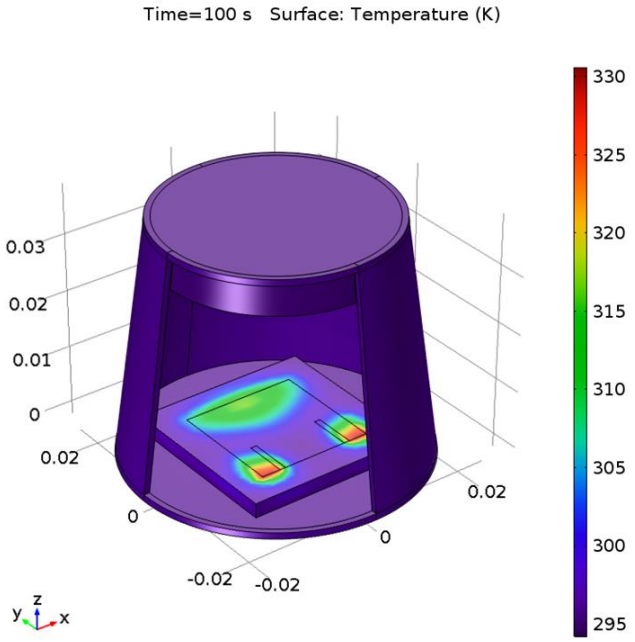

Figure 3.17 - Temperature plots of a 1/4 scale wide top resonant cavity model.

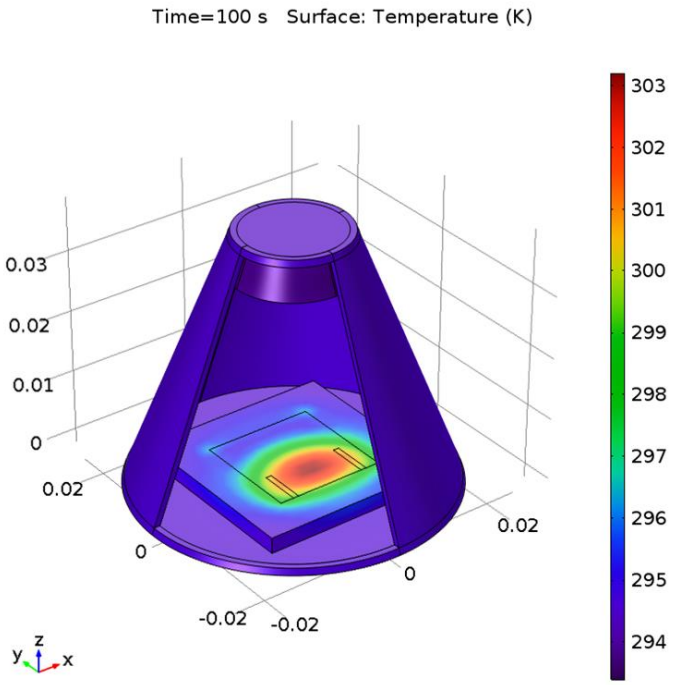

Figure 3.18 - Temperature plots of a 1/4 scale narrow top resonant cavity model.

The temperature results in the ¼ scale models are similar to the results of the ½ scale model. The highest rise in temperature occurs in the micropatch antenna with rises of temperature of lower magnitude occurring in the Teflon insert. The copper skin of the cavities all rose uniformly between 2 – 3 K. The temperature on the micropatch antennas of the ¼ scale model rose to ~309 K, the temperature on the micropatch antenna of the ¼ scale wide top model encountered a much higher rise of 37 K to ~330 K in two locations on the reflecting side of the antenna on the same side as the feed input. On the opposite side of the antenna, there was a more subdued temperature rise of 24 K to ~318K. The ¼ scale narrow top model had much lower temperatures than the wide top model, its highest temperature occured in the micropatch antenna and was ~304K.

The temperature increases that were computationally modeled are in good agreement

with previously performed experiments. Two authors have published papers discussing the heating of the cavity. These papers were published by M. Tajmar of TU Dresden, and H.G. White of NASA Eagleworks Labs [33], [34], [37]. Their experimental setups are discussed in the Introduction chapter and have descriptions of their test articles and instrumentation. NASA Eagleworks ran a cavity at 40, 60, and 80 W for approximately 1 minute. They saw similar rises in temperature in their cavities and associated electronics. A IR camera image from their experiment is shown in Figure 3.19 [34].

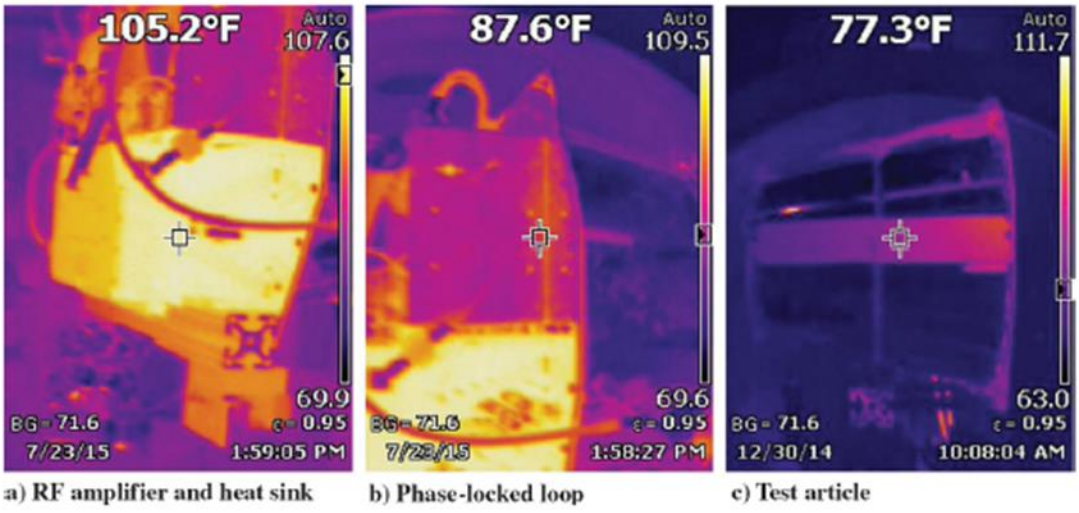

Figure 3.19 - IR Camera image taken of NASA Eagleworks Cavity test article [34].

Tajmar reported similar findings, although the power output of his test equipment is much higher than used by the Eagleworks lab. Tajmar's RF power output was 700 W and he recorded a temperature rise of 35 K in his cavity [37].

The temperature rises plotted in the previous figures are a direct result of both volume and surface resistive losses throughout the model. These losses come in the form of dielectric loss tangent losses in the Teflon insert and micropatch antenna substrate, and resistive surface

losses in the copper cavity walls. Both volume and surface losses for the ½ scale resonant cavity models are displayed in Figures 3.20, 3.21, and 3.22. The ½ scale models were simulated for 250 s. The plots are shown with transparent boundaries so that the interior may be viewed.

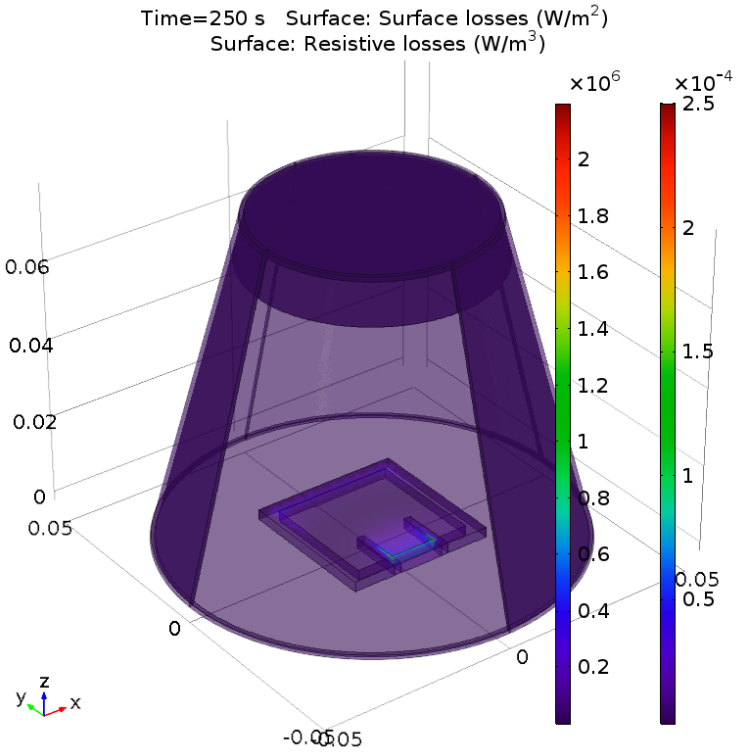

Figure 3.20 - Surface losses and resistive losses for a 1/2 scale resonant cavity model.

The loss plots shown mirror the temperature plots shown previously in this chapter. The locations of higher resistive losses correspond to the locations of highest temperature. The surface conductive losses are seen to be dispersed over the geometry of the cavity, just as the temperature was mostly homogenous throughout the copper cavity. Due to the surface area to volume ratio of the cavities, the units of losses are non-intuitive. The unit scale for the resistive

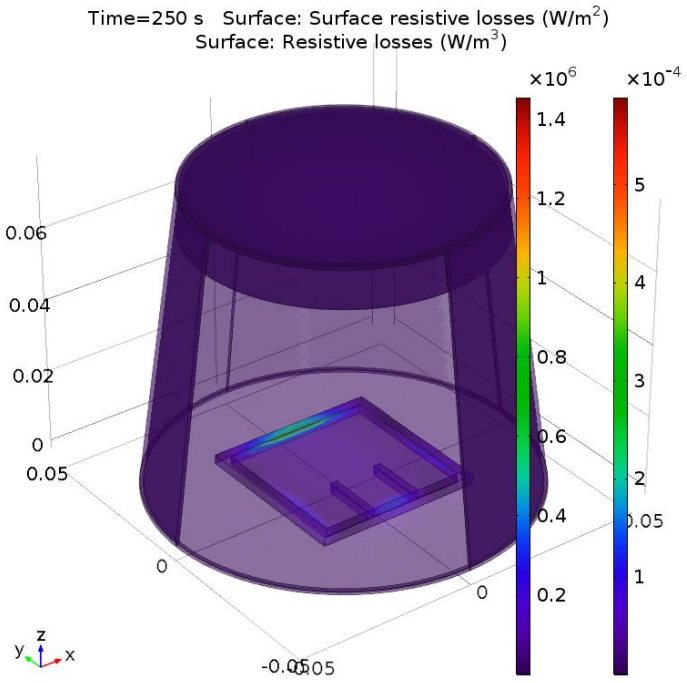

Figure 3.21 - Surface losses and resistive losses for a 1/2 scale wide top resonant cavity model.

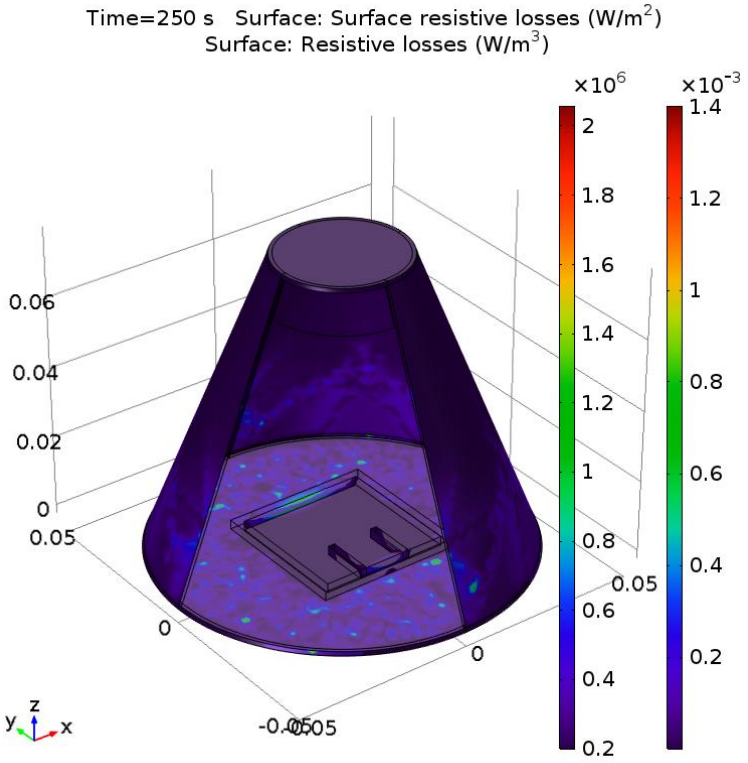

Figure 3.22 - Surface losses and resistive losses for a 1/2 scale narrow top resonant cavity model.

losses are on the left and the surface losses are on the right. Also apparent is the difference in magnitude between the two losses. It will be shown in the presentation of global evaluations that the volume resistive losses are much higher than the surface resistive losses.

Similar plots were taken for the ¼ scale resonant cavity models. These surface plots have a portion of the cavity wall hidden in order to show the micropatch antenna on the interior and are displayed in Figures 3.23, 3.24, and 3.25.

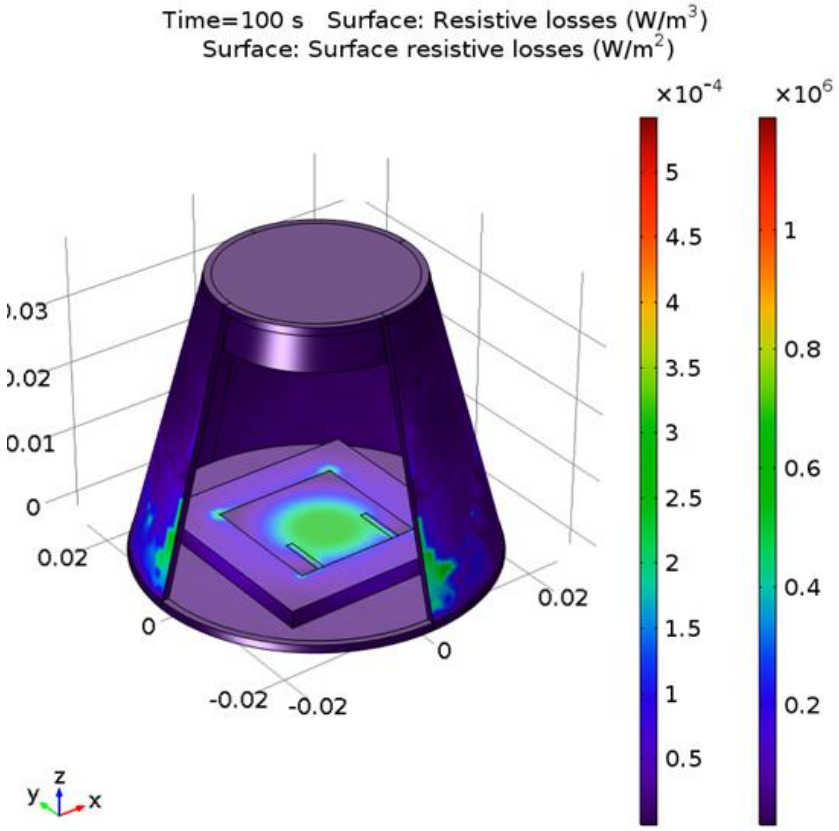

Figure 3.23 - Surface losses and resistive losses for a 1/4 scale resonant cavity model.

Very similar to the results discussed for the ½ scale model resonant cavities. The ¼ scale models also display the coupling between RF losses and input heat transfer. The locations that saw the highest rise in temperature also saw the highest density of RF losses.

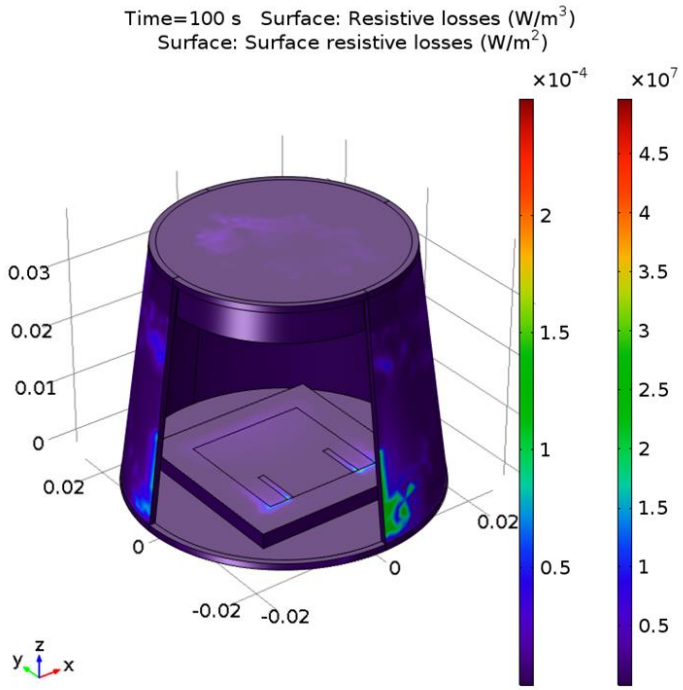

Figure 3.24 - Surface losses and resistive losses for a 1/4 scale wide top resonant cavity model.

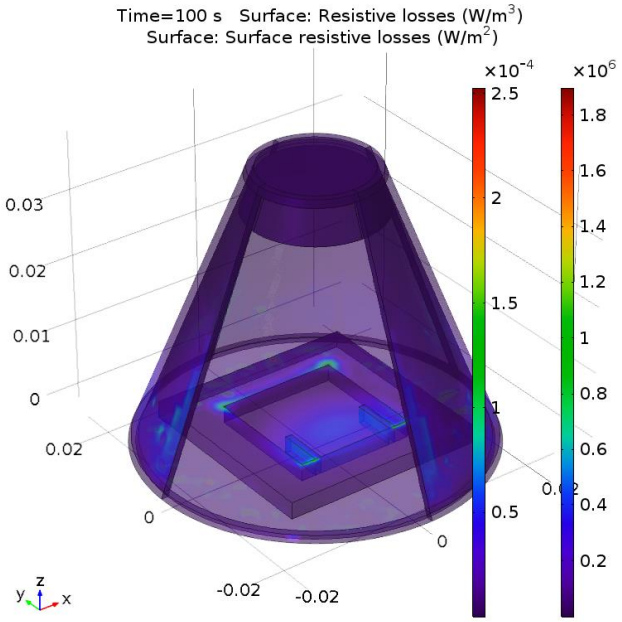

Figure 3.25 - Surface losses and resistive losses for a 1/4 scale narrow top resonant cavity model.

Another feature of the surface losses plot that should be mentioned are that the results of the surface resistive losses are highly dependent on mesh density. The surface resistive losses display a magnitude that is periodic dependent on the size of the mesh used. This behavior is shown in Figure 3.26.

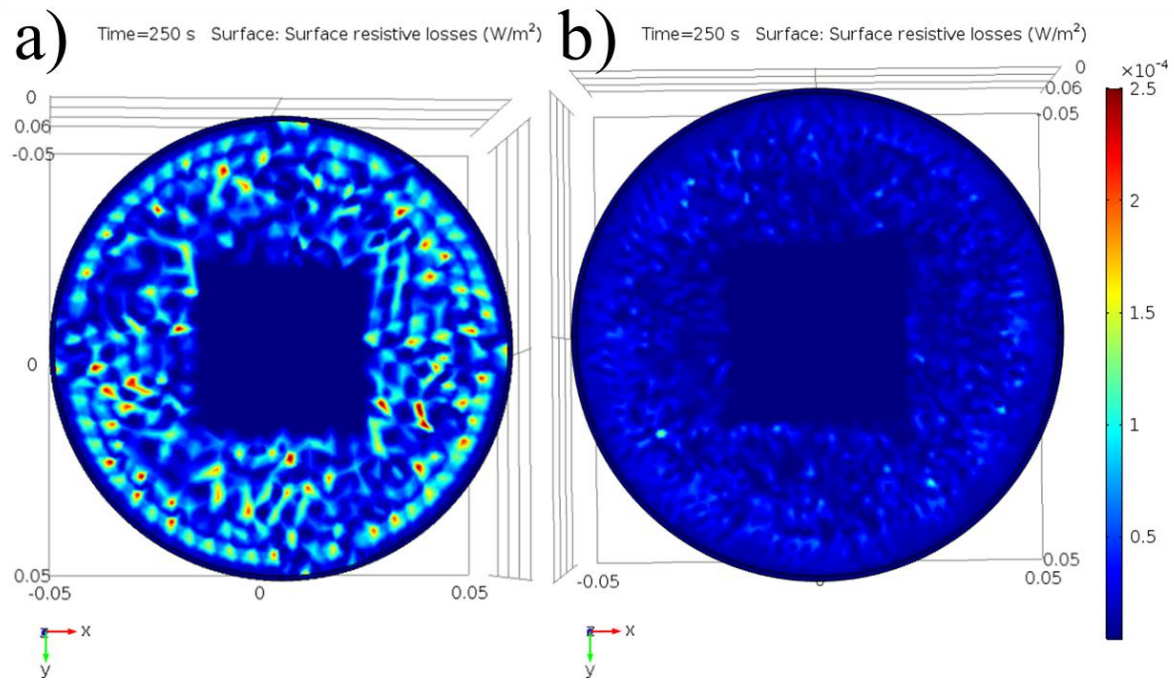

Figure 3.26 - Surface losses on the bottom of the resonant cavity, below the micropatch antenna. Model computed with: a) a coarse mesh (10k mesh units), b) a high-density mesh (100k mesh units).

As can be seen in the figure, the lower the mesh density, the more localized and higher the losses are. Although part a) of Figure 3.26 shows higher intensities of surface losses, the magnitude between the two parts of the figure are nearly equivalent. It can be thought that increasing the mesh density smooths the losses towards their eventual physical solution. It can be inferred from the Figure 3.26 that the surface losses in reality would smoothly develop as a function of the magnitude of the electric field impinging on the boundary.

Another notable feature displayed in Figure 3.26 is the lossless square in the center of the cavity. As described in the Experimental Methods chapter, this lossless square is due to the boundary conditions necessary to construct the micropatch antenna in COMSOL's modeling environment. The ground plane and patch of the antenna must be modeled as perfect electric conductors and, therefore, encounter no loss. In a real-world model, this area would also contribute to surface losses and heating. This is a part of the simulation that will introduce error into the solution when compared to its physical counterpart. Another portion of the simulation that leads to error is the lack of simulated surface roughness. Surface roughness can as much as double the surface resistivity of conductive metals when the minimum surface roughness is roughly equivalent to the skin depth [47]–[49]. The skin effect of the cavities in this research was calculated to range between 0.8 – 1.3 μm; this corresponds to the minimum surface roughness that can be expected for machining and deposition processes. A result of this is that the surface losses would double. Even with this correction, volume resistive losses due to the dielectric materials in the cavity are by far the dominant mode of losses for the resonant cavity.

As discussed in the Experimental Methods chapter, global evaluations were made of the quality factor, energy contained in the electric field, surface resistive losses, and volume resistive losses. While the surface plots shown in Figures 3.20 – 3.26 give a good geometrical understanding of the distribution of losses, it does a poor job of representing the magnitude of each factor considered. Table 3.1 displays these values for all six resonant cavities simulated.

The quality factor for the ½ scale model resonant cavities ranges between 50,000 – 100,000. The quality factor for the ¼ scale model is lower than the ½ scale model, ranging approximately from 14,500 to 31,000. This can be attributed to the much larger volume by percentage of dielectric components within the ¼ scale model resonant cavities. As can be seen

in the table, the losses due to volume resistivity of the dielectric components within the cavity are roughly one million times the magnitude of the surface losses. This agrees with the temperature and loss plots.

Table 3.1 - Global Evaluations computed for all six resonant cavities simulated.

	Quality Factor	Energy in the Electric Field [μJ]	Surface Losses [μW]	Dielectric Losses [W]
1/2 Size Narrow Top Cavity	108100	5.762	0.7582	0.94421
1/2 Size Scale Cavity	58013	1.039	0.12337	0.30394
1/2 Size Wide Top Cavity	51878	7.4476	0.83322	2.257
1/4 Size Narrow Top Cavity	21941	0.27621	0.05426	0.4469
1/4 Size Scale Cavity	30919	0.7739	0.14944	0.85109
1/4 Size Wide Top Cavity	14491	0.63975	0.077973	1.3884

Chapter 4: Conclusion

A thought experiment comparing a hypothetical space propulsion system that requires no thrust to contemporary options for space propulsion was introduced. This outlined the possible benefits and drawbacks of such a system. The previous work testing devices that possibly behave like the hypothetical thruster was then introduced and discussed. These thrusters are called Q-thrusters or EM Drives in the current literature. From this work, the possible theories of operation of a Q-thruster were discussed as well as the design and physics governing the operation of the device as an RF resonant cavity.

Informed by the previous work conducted, a research plan was developed to simulate several cavities similar to those that had been tested experimentally. Verification of COMSOL computational output against known analytical results were conducted. This verification used Matlab scripts to create analytical results directly from COMSOL data output. The analytical models that were compared to COMSOL simulations were the analytical models for rectangular, cylindrical, and spherical resonant cavities. The rectangular and cylindrical COMSOL simulations had a very high amount of agreement to the analytical models. However, the spherical COMSOL simulation had a high amount of disagreement with the analytical models. Attempts were made to discern what was causing the disagreements between spherical solution and its analytical counterpart. These included varying mesh densities, altering COMSOL solver settings, and isolating planar data. The rectangular and cylindrical resonant cavities were also modeled to be driven by micropatch antennas. This computational model was created in order to test the behavior of cavities driven by antennas. In particular it was desired to know if the dominant electric field shape inside the cavity would be the resonant mode of the cavity or the

radiation pattern of the antenna. These antenna driven cavities showed that the resonant mode of the cavity was the dominant field shape.

After verifying the accuracy of COMSOL to known analytical solution, simplified models of the cavities were made in order to find the eigenfrequencies at which the cavities would be operating. These eigenfrequencies were then used in another Matlab script that automatically designed a micropatch antenna based on user input. These micropatch antennas were used to create six resonant cavity Multiphysics models in COMSOL. The process of building this model in COMSOL was discussed in depth. From these COMSOL models, microwave heating simulations were carried out. The data exported from these solutions includes electric field magnitude, temperature, RF surface losses, RF volume losses, Quality Factor, and total energy contained in the electric field. These results were then compared to the experimental results that have been conducted at other institutions.

References:

[1] "Alternatives for Future U.S. Space-Launch Capabilities," Congressional Budget Office, Washington D.C., 2006.

[2] J. W. Dunning, S. Benson, and S. Oleson, "An Overview of NASA's Electric Propulsion Program," in *27th International Electric Propulsion Conference*, 2001, pp. 63–92.

[3] National Aeronautics and Space Administration, "NASA Technology Roadmaps TA 2: In-Space Propulsion Technologies," 2015.

[4] National Aeronautics and Space Administration, "NASA Technology Roadmaps TA 1: Launch Propulsion Systems," 2015.

[5] R. M. Myers, S. R. Oleson, F. M. Curran, and S. J. Schneider, "Small Satellite Propulsion Options Services," in *30th AIAA/ASME/SAE/ASEE Joint Propulsion Conference*, 1994, p. AIAA-94-2997.

[6] D. Platt, "A Monopropellant Milli-Newton Thruster System for Attitude Control of Nanosatellites," in *Proceedings of the 16th Annual USU Conference on Small Satellites*, 2002, pp. 1–6.

[7] H. Jung, J. H. Kim, J. S. Kim, and X. Nh, "Test and Evaluation of a 70 N-class Hydrazine Thruster for Application to the Precise Attitude Control of Space Vehicles," in *49th AIAA/ASME/SAE/ASEE Joint Propulsion Conference*, 2013, pp. 1–10.

[8] S. K. Stephens, "The Juno mission to Jupiter: Lessons from cruise and plans for orbital operations and science return," *IEEE Aerosp. Conf. Proc.*, vol. 2015–June, pp. 1–20, 2015.

[9] C. Soares, H. Barsamian, and S. Rauer, "Thruster plume induced contamination measurements from the PIC and SPIFEX flight experiments," in *International Symposium on Optical Science and Technology*, 2002, pp. 1–11.

[10] D. Estublier and C. Koppel, "SMART-1 EPS End-to-End Test: Final Results & Lessons Learnt," in *Proceedings of the International Electric Propulsion Conference*, 2003, pp. 1–9.

[11] C. R. Koppel and D. Estublier, "The SMART-1 hall effect thruster around the moon: In flight experience," *29th Int. Electr. Propuls. Conf.*, pp. 1–9, 2005.

[12] H. Kuninaka, K. Nishiyama, I. Funaki, T. Yamada, Y. Shimizu, and J. Kawaguchi, "Powered might of electron cyclotron resonance ion engines on Hayabusa explorer," *J. Propuls. Power*, vol. 23, no. 3, pp. 544–551, 2007.

[13] V. Kim, G. Popov, B. Arkhipov, V. Murashko, O. Gorshkov, A. Koroteyev, V. Garkusha, A. Semenkin, and S. Tverdokhlebov, "Electric Propulsion Activity in Russia," in *27th International Electric Propulsion Conference*, 2001, pp. 1–5.

[14] S. Jansen, H. Helvajian, and K. Breuer, "Micropropulsion Systems for Aircraft and Spacecraft," in *Microengineering for Aerospace Systems*, 1999, pp. 657–696.

[15] J. Rushby and J. Crow, "Evaluation of an expert system for fault detection, isolation, and recovery in the manned maneuvering unit," 1990.

[16] A. Huang, S. Janson, W. Hansen, L. Steffeney, and H. Helvajian, "A Mass-Producible Glass / Ceramic Micropropulsion Unit for a Co-Orbiting Satellite Assistant (COSA) Mission," in *Small Satellites: Past, Present, and Future*, H. Helvajian and S. Janson, Eds. El Segundo, CA: The Aerospace Press, 2003, pp. 559–592.

[17] M. Mihailovic, T. V. Mathew, J. F. Creemer, B. T. C. Zandbergen, and P. M. Sarro, "MEMS silicon-based resistojet micro-thruster for attitude control of nano-satellites," *2011 16th Int. Solid-State Sensors, Actuators Microsystems Conf. TRANSDUCERS'11*, pp. 262–265, 2011.

[18] R. S. Jankovsky, J. M. Sankovic, and S. Oleson, "Performance of a FAKEL K10K Resistojet," *33rd Jt. Propuls. Conf. Exhib.*, p. 14, 1997.

[19] F. Martel, L. Perna, and P. Lozano, "Miniature Ion Electrospray Thrusters and Performance Tests on CubeSats," *26th Annu. AIAA/USU Conf. Small Satell.*, pp. 1–6, 2012.

[20] D. Spence, E. Ehrbar, N. Rosenblad, N. Demmons, T. Roy, S. Hoffman, D. Williams, and V. Hruby, "Electrospray Propulsion Systems for Small Satellites," in *27th Annual AIAA/USU Smallsat Conference*, 2013, pp. 1–7.

[21] R. L. Burton and P. J. Turchi, "Pulsed Plasma Thruster.pdf," *J. Propuls. Power*, vol. 14, no. 5, pp. 716–735, 1998.

[22] J. H. Gilland, M.R. LaPointe, S. Oleson, C. Mercer, E. Pencil, and L. Mason, "MW-Class Electric Propulsion System Designs for Mars Cargo Transport," in *AIAA SPACE 2011 Conference and Exposition*, 2011, pp. 1–15.

[23] D. Milligan, O. Camino, and D. Gestal, "SMART-1 Electric Propulsion: An Operational Perspective," *SpaceOps 2006 Conf.*, pp. 1–15, 2006.

[24] T. Roy, V. Hruby, N. Rosenblad, P. Rostler, and D. Spence, "CubeSat Propulsion using Electrospray Thrusters," in *23rd Annual AIAA/USU Conference on Small Satellites*, 2009, pp. 1–11.

[25] L. F. Velásquez-García, A. I. Akinwande, and M. Martínez-Sánchez, "A planar array of

micro-fabricated electrospray emitters for thruster applications," *J. Microelectromechanical Syst.*, vol. 15, no. 5, pp. 1272–1280, 2006.

[26] B. Gassend, L. F. Velásques-García, and A. I. Akinwande, "Mechanical Assembly of Electrospray Thruster Grid," in *Proceedings of the International Electric Propulsion Conference 2005 (IEPC05)*, 2005, pp. 1–12.

[27] V. V Zhurin, H. R. Kaufman, and R. S. Robinson, "Physics of closed drift thrusters," *Plasma Sources Sci. Technol.*, vol. 8, no. 1, pp. R1–R20, 1999.

[28] J. P. Boeuf and L. Garrigues, "Low frequency oscillations in a stationary plasma thruster," *J. Appl. Phys.*, vol. 84, no. 7, p. 3541, 1998.

[29] A. I. Morozov, "The Conceptual Development of Stationary Plasma Thrusters," *Plasma Phys. Reports*, vol. 29, no. 3, pp. 235–250, 2003.

[30] M. Martinez-Sanchez and J. E. Pollard, "Spacecraft Electric Propulsion-An Overview," *J. Propuls. Power*, vol. 14, no. 5, pp. 688–699, 1998.

[31] J. Kohler, J. Bejhed, H. Kratz, F. Bruhn, U. Lindberg, K. Hjort, and L. Stenmark, "A hybrid cold gas microthruster system for spacecraft," *Sensors Actuators, A Phys.*, vol. 97, no. 98, pp. 587–598, 2002.

[32] R. W. Ridenoure, R. Munakata, S.D. Wong, A. Diaz, D.A. Spencer, D.A. Stetson, B. Betts, B.A. Plante, J.D. Foley, and J.M. Bellardo, "Testing The LightSail Program: Advancing Solar Sailing Technology Using a CubeSat Platform," *J. Small Satell.*, vol. 5, no. 2, pp. 531–550, 2016.

[33] D. Brady, H. G. White, P. March, J. T. Lawrence, and F. J. Davies, "Anomalous Thrust Production from an RF Test Device Measured on a Low-Thrust Torsion Pendulum," *50th AIAA/ASME/SAE/ASEE Jt. Propuls. Conf.*, pp. 1–21, 2014.

[34] H. White, P. March, J. Lawrence, J. Vera, A. Sylvester, D. Brady, and P. Bailey, "Measurement of Impulsive Thrust from a Closed Radio-Frequency Cavity in Vacuum," *J. Propuls. Power*, pp. 1–12, 2016.

[35] H. White, P. March, J. Lawrence, J. Vera, A. Sylvester, D. Brady, and P. Bailey, "Anomalous Impulsive Thrust Production from an RF Test Device Measured in Hard Vacuum Conditions on a Low-Thrust Torsion Pendulum," in *51st AIAA/ASME/SAE/ASEE Joint Propulsion Conference*, 2015, pp. 1–38.

[36] H. G. White and P. March, "Advanced Propulsion Physics: Harnessing the Quantum Vacuum.," *Nucl. Emerg. Technol. Sp.*, pp. 1–2, 2012.

[37] G. F. M. Tajmar, "Direct Thrust Measurements of an EM Drive and Evaluation of Possible Side-Effects," in *51st AIAA/SAE/ASEE Joint Propulsion Conference*, 2015, pp.

4083–4093.

[38] M. N. Yang Juan, Yang Le, Zhu Yu, “Applying Method of Reference 2 to Effectively Calculating Performance of Microwave Radiation Thruster,” *J. Northwest. Polytech. Univ. Vol 28 No 6 Dec 2010*, vol. 28, no. 6, pp. 1–11, 2010.

[39] R. Shawyer, “Second generation EmDrive propulsion applied to SSTO launcher and interstellar probe,” *Acta Astronaut.*, vol. 116, pp. 166–174, 2015.

[40] G. P. Fetta, “Electromagnetic thruster,” US20140013724 A1, 2011.

[41] H. G. White, P. March, and N. Williams, “Eagleworks Laboratories: Advanced Propulsion Physics Research,” 2012.

[42] COMSOL, *COMSOL 5.2 User’s Guide*. Burlington, MA: COMSOL, Inc., 2015. (www.comsol.com)

[43] A. Mehrparvar, D. Pignatelli, J. Carnahan, R. Munakata, W. Lan, A. Toorian, A. Hutputanasin, and S. Lee, “Cubesat design specification (CDS) REV 13.” The CubeSat Project, San Luis Obispo, CA, pp. 1–42, 2014.

[44] D. M. Pozar, *Microwave Engineering*, 3rd ed. John Wiley & Sons, 2005.

[45] W. L. Stutzman and G. A. Thiele, "Chapter 11 Low-Profile Antennas and Personal Communication Antennas," in *Antenna Theory and Design*, Hoboken, NJ, 3rd ed. John Wiley & Sons, 2013, pp. 465–535.

[46] M. A. Matin and A. I. Sayeed, “A design rule for inset-fed rectangular microstrip patch antenna,” *WSEAS Trans. Commun.*, vol. 9, no. 1, pp. 63–72, 2010.

[47] R. G. Chambers, “The anomalous skin effect,” *Proc. R. Soc. London A Math. Phys. Eng. Sci.*, vol. 215, no. 1123, pp. 481–497, 1952.

[48] A. B. Pippard and L. Bragg, “The surface impedance of superconductors and normal metals at high frequencies II. The anomalous skin effect in normal metals.,” *Proc. R. Soc. London A Math. Phys. Eng. Sci.*, vol. 191, no. 1026, pp. 385–399, 1947.

[49] S. P. Morgan, “Effect of surface roughness on eddy current losses at microwave frequencies,” *J. Appl. Phys.*, vol. 20, no. 4, pp. 352–362, 1949.

Appendix A: Eigenproblem Matlab scripts

```
% Analytical solutions to eigenfrequencies and electric field distributions
% of a rectangular prism

% Josh Pennington 2/16/17

clear; clc;

a = 5e-2;%input('input width of the prism in m \n'); % Dimensions of the prism
b = 5e-2;%input('input depth of the prism in m \n');
h = 5e-2;%input('input height of the prism in m \n');

index = 100; % determines the size of the matrix to be computed.
A = -78.913887; %voltage input for electric field 1 is normalized.

m = input('input the m index (1,2,3,. . .) \n'); % TE indices mnl
n = input('input the n index (1,2,3,. . .) \n');
l = input('input the l index (0,1,2,. . .) \n');

c = 3e8; % speed of light in m/s

fmnl = (c/(2*pi))*sqrt((((m*pi)/a)^2)+(((n*pi)/b)^2)+(((l*pi)/h)^2)); % Eigenfrequency of the m n
l mode

fprintf('The eigenfrequency of the TE %d %d %d mode is %d Hz \n',m,n,l,fmnl) % display

N = load('F:\COMSOL Files\Masters Thesis\COMSOL 2017-05-25\5cmCubeoutput.txt'); % Inputs values
from COMSOL (Mesh and Ez values)
%N = load('F:\COMSOL Files\Masters Thesis\COMSOL 2017-05-25\5cmCubeGridOutput.txt'); % Same
%thing, but with values arranged in a grid

amat = N(:,1); % Setting up integration limits based on COMSOL mesh
bmat = N(:,2);
hmat = N(:,3);

EzCOMSOL = N(:,4); % Imported Ez from COMSOL

Ez = zeros(length(EzCOMSOL),1); % Setting up Electric field matrix for MATLAB solution

for i = 1:length(amat)-1
   Ez(i) = A*sin((m*pi*amat(i))/a)*sin((n*pi*bmat(i))/b)*cos((l*pi*hmat(i))/h); %Analytical
solver for input location values form COMSOL
end

check = (Ez-EzCOMSOL)./Ez;
ind = 1;

for j = 1:length(check)-1 % Sorts data from a matrix that falls within a certain range and puts
it into a new matrix for ease of statistics
    if check(j) > -0.5 && check(j) < 0.5 % Should make this into a function (import everything
into Python Spyder?)
        stdevcheck(ind) = check(j);
        ind = ind + 1;
    end
end

meanrec = mean(stdevcheck);
stdrec = std(stdevcheck);

fprintf('The agreement between COMSOL and the analytical solutions is %d +/- %d \n', meanrec,
stdrec) %display's statistical info

set(gcf, 'color', 'w')
plot(hmat, check);
title('Comparison between the Electric Fields from COMSOL and Analytic solutions')
xlabel(' Span of Z-axis from 0 to 5 cm [m]')
ylabel(' Percent difference between Analytical and COMSOL solutions [unitless]')
```

```
axis([0 0.05 -0.5 1])



% Analytical solutions to eigenfrequencies and electric field distributions
% of a cylinder

% Josh Pennington 2/25/17

clear; clc;

%N = load('F:\COMSOL Files\Masters Thesis\COMSOL 2017-05-25\5cmCylinderGridoutput.txt');
N = load('F:\COMSOL Files\Masters Thesis\COMSOL 2017-05-25\5cmCylinderoutput.txt'); % NOTE:
Cylinder must have center at (x,y) = (0,0)
% so that the radius = sqrt(x^2 + y^2), otherwise eqn in line 35 must be
% changed to reflect the shift in origin.

x = N(:,1); % Loads mesh parameters from COMSOL, coordinates are unordered.
y = N(:,2);
z = N(:,3);

EzCOMSOL = N(:,4); % loads Electric field in the z direction from COMSOL. nth component of Ez
corresponds to x(n) y(n) and z(n)

a = 5e-2;%input('input radius of the cylinder in m \n'); % Dimensions of the cylinder
h = 5e-2;%input('input height of the cylinder in m \n');

bess = [2.4048 5.5201 8.6537 11.791534439 14.9309]; % Roots of the 0 order bessel function

Ez = zeros(length(EzCOMSOL),1); % MATLAB solution based on analytical equation

A = 393.7; % Normalization constant for analytical solution
c = 3e8; % Speed of light in m/s

n = input('input the n index (1,2,3,. . .) \n'); % TE indices nl
l = input('input the l index (0,1,2,. . .) \n');

fnl = (c/(2*pi))*sqrt((bess(n)/a)^2+((l*pi)/h)^2); % Eigenfrequency of the m n l mode

fprintf('The eigenfrequency of the TM %d %d mode is %d Hz \n',n,l,fnl) % display

for i = 1:length(EzCOMSOL)-1
    Ez(i) = A*besselj(0,(bess(n)*(sqrt(x(i)^2+y(i)^2)/a)))*cos(((l*pi*z(i))/h));
end

check = (Ez-EzCOMSOL)./Ez;
ind = 1;

for j = 1:length(check)-1 % Sorts data from a matrix that falls within a certain range and puts
it into a new matrix for ease of statistics
    if check(j) > -0.5 && check(j) < 0.5 % Should make this into a function (import everything
into Python Spyder?)
        stdevcheck(ind) = check(j);
        ind = ind + 1;
    end
end

meancyl = mean(stdevcheck);
stdcyl = std(stdevcheck);

fprintf('The agreement between COMSOL and the analytical solutions is %d +/- %d \n', meancyl,
stdcyl) %display's statistical info

set(gcf, 'color', 'w')
plot(x, check);
title('Comparison between the Electric Fields from COMSOL and Analytic solutions (Cylinder)')
xlabel(' Span of Z-axis from 0 to 5 cm [m]')
ylabel(' Ez Matlab/Ez COMSOL [unitless]')
axis([0 0.05 -0.5 1])
```

```
% Analytical solutions to eigenfrequencies and electric field distributions
% of a sphere

% Josh Pennington 2/27/17

clear; clc;

N = load('F:\COMSOL Files\Masters Thesis\COMSOL 2017-05-25\5cmSphereoutput2.txt'); % Input values
from COMSOL
%N = load('F:\COMSOL Files\Masters Thesis\COMSOL 2017-05-25\5cmSphereGridoutput.txt')

x = N(:,1); % loads the coordinates used in COMSOL calculations
y = N(:,2);
z = N(:,3);

EzCOMSOL = N(:,4); % Loads the COMSOL solutions to the z electric field

a = 5e-2;%input('input radius of the sphere in m \n'); % Dimensions of the sphere

A = 1050; %voltage input for electric field 1 is normalized.

n = input('input the n index (1,2,3,. . .) \n'); % TM indices nl
l = input('input the l index (0,1,2,. . .) \n');

bess = [2.405 5.520 8.654 11.79 14.9309]; % Zeroth order Bessel function zeros

c = 3e8; % speed of light in m/s

fnl = (c*bess(n))/(2*pi*a); % Eigenfrequency

fprintf('The eigenfrequency of the TM %d %d mode is %d Hz \n',n,l,fnl) % display

k = (n*pi)/a;

r = zeros(length(x),1);

for i = 1:length(EzCOMSOL)
    r(i,1) = sqrt(x(i)^2+y(i)^2+z(i)^2);
    Ez(i,1) = A*sin(k*r(i))/(k*r(i));
end

check1 = EzCOMSOL./Ez;
check = (Ez-EzCOMSOL)./Ez;
ind = 1;

for j = 1:length(check)-1 % Sorts data from a matrix that falls within a certain range and puts
it into a new matrix for ease of statistics
    if check(j) > -3 && check(j) < 0.5 % Should make this into a function (import everything into
Python Spyder?)
        stdevcheck(ind) = check(j);
        ind = ind + 1;
    end
end

meansph = mean(stdevcheck);
stdsph = std(stdevcheck);

fprintf('The agreement between COMSOL and the analytical solutions is %d +/- %d \n', meansph,
stdsph) %display's statistical info

set(gcf, 'color', 'w')
%plot(x, check);
%title('Comparison between the Electric Fields from COMSOL and Analytic solutions (Sphere)')
%xlabel(' Span of Z-axis from 0 to 5 cm [m]')
%ylabel(' Percent difference between Analytical and COMSOL solutions [unitless]')
%axis([0 0.05 -0.5 1])

plot(r, Ez, r, EzCOMSOL);
```

```
title('Comparison between Analytical Ez and COMSOL generated Ez')
xlabel(' Radius of sphere [m]')
ylabel(' Electric Field [V/m]')
```

Appendix B: Micropatch antenna dimensional solver Matlab script

```
% Micropatch Antenna Dimensional Solver
% Josh Pennington 1/18/17
% Updated 3/9/17 - added section to design impedance tuning stubs and
% creating a 50 ohm feed trace transmission line.

clear; clc;

f = input('input the resonant frequency of the system in Hz \n'); % Resonant Frequency of cavity
in Hz
t = input('input the thickness of the subtrate in m \n'); % Substrate thickness in m
T = input('input the trace thickness - 1oz copper is 35.56e-6 m, 2oz is 71.12e-6 m \n'); % Trace
thickness in m
c = 3e8; % Speed of light in m/s
lamb = c/f; % Wavelength in m
er = input('input the relative permittivity of the substrate \n'); % relative permittivity of
dielectric substrate


L = 0.49*(lamb/sqrt(er)) % Length of microstrip patch in m
%Za = input('input the characteristic impedance of the system design \n'); %Desired input
impedance of the micropatch antenna in Ohms
%W = (L/sqrt(Za))*sqrt(90)*sqrt((er^2/(er-1))) % Width of the micropatch antenna in m
W = L;
Za = 90*(er^2/(er-1))*(L/W)^2 %Input impedance if dimensions are controlling design requirements.
Bw = 3.77*((er-1)/er^2)*(W/L)*(t/lamb) % Bandwidth of the micropatch antenna in % of center
frequency when VSWR is less than 2:1

% Calculation of impedance notch dimensions
xi = (L/pi)*acos(sqrt(50/Za)) % calculates notch depth for a 50 ohm impedance system
yi = L/20 %#ok<*NOPTS> % design choice for notch width

% Calculation of trace transmission line width (for impedance)

B = (377*pi)/(2*50*sqrt(er));
tw = t*(2/pi)*(B - 1 - log(2*B - 1)+((er - 1)/2*er)*(log(B - 1) + 0.39 -(0.61/er))) % 50 Ohm
Transmission feed line calculator
```

Appendix C: Description of Research for Popular Publication.

The field of space propulsion is vital for the operation of daily modern life. Cell phones, television, GPS, and the internet all depend on a highly functional array of satellites in orbit around the Earth. Depending on the orbit, these satellites needs propulsion systems to keep from burning up in Earth's atmosphere. The fuel requirements of all modern thrusters lead to a hard lifetime limit on all spacecraft before they become inoperative. Fuel requirements are also a major design bottleneck for interplanetary scientific probes. Low maneuverability due to fuel constrictions often makes it necessary to take long circuitous trajectories that take advantage of gravity assists from other planets as checkpoints on the way to its final goal. While the necessity of swinging by other planets offers invaluable scientific data, it comes at the cost of expediency. The journey of interstellar probes destined for the outer solar system can take nearly a decade.

A driving developmental goal for space propulsion engineers has been increasing the efficiency of propulsion. Extracting as much work as possible out of every gram of fuel. For these reasons, the idea of a propulsion system that could produce thrust without the necessity of fuel has always been an ideal prospect. The EM-Drive or Q-thruster is a device that possibly meets those hallmarks. The device consists of a closed resonant cavity shaped like a truncated cone with a dielectric like Teflon inserted at one end. Since approximately 2005, work by several international companies and labs, including NASA, have shown positive thrust test results of varying magnitude. These results are intriguing and merit further investigation of the phenomena, but it should be noted that not all possible sources of experimental error have been eliminated. Also notable is that while there have been hypotheses presented to explain the thrust, none align with the currently held understanding of our physical world. The state of research into this phenomenon can therefore be said to be in an infant stage.

Because dedicated research into the subject of the Q-thruster phenomena is only just beginning, there exists an opportunity to make a large impact towards greater understanding of the device. This drove Josh Pennington's (graduate student in the Microelectronics-Photonics program at the University of Arkansas) decision to focus on the Q-thruster resonant cavities for his M.S. thesis.

The majority of this work was conducted using a software called COMSOL Multiphysics. The software allows for complex systems to be simulated in a Multiphysics environment. Microwave heating models were designed and created for six resonant cavities that were alterations on the design used by NASA Eagleworks Labs. Because a prime suspect of possible erroneous thrust data is the heating of the cavity due to microwaves, temperature information was recorded. Also recorded were several microwave parameters such as electric field strength, quality factor, and RF losses.

Appendix D: Executive Summary of Newly Created Intellectual Property

The following description of new intellectual property was created in the course of this research project and should be considered from both a patent and commercialization perspective.

1. Novel computational models of several geometries of resonant microwave cavity thrusters. Including frequency domain electromagnetic and transient heat transfer modeling of the thruster device.

Appendix E: Potential Patent and Commercialization Aspects of Listed Intellectual Property Items

E.1 Patentability of Intellectual Property

The IP listed in Appendix D is not considered patentable. The computational method that was used consisted of known physics developed on a proprietary commercial third-party software (COMSOL). The novelty exists due to the nascent nature of the devices and research. They would not meet the qualification of a “non-obvious” solution to a practitioner in the field.

E.2 Commercialization Prospects

Not applicable

E.3 Possible Prior Disclosure of IP

Not applicable

Appendix F: Broader Impact of Research.

F1: Applicability of Research Method to Other Problems

The research conducted highly depended on the use of computational aids like COMSOL Multiphysics and Matlab. These platforms are useful across all engineering disciplines. COMSOL provides a Multiphysics simulation environment that simulate extremely diverse physical models. For this research, the RF and Heat Transfer modules were used. These could be used to model anything from a cell phone antenna to a cancer treatment method. Matlab is also a programming environment that is useful across all engineering and scientific disciplines. Its matrix driven approach is perfect for presenting, analyzing, and performing operations on large datasets

F2: Impact of Research on U.S. and Global Society

The use of satellites has become an integral part of global society. Satellites are necessary for such tasks as accurate prediction of the weather and global telecommunication. Satellites are still extremely expensive to launch and current propulsion systems lead to a limited lifetime of operation for most satellites. If the research results in the development of a useful thruster that produces thrust without the need for fuel, the lifetime of satellites could be extended greatly.

F3: Impact of Research Results on the Environment

Impact on the environment is expected to be null to minimal. The research was conducted in a computational environment, no real-world models have yet been constructed. When constructed, the models will be built out of non-toxic materials and if successful will be in space, and not even in the environment any longer. If the research progresses to the point where devices are tested in a space environment, NASA requires an end of life plan for all spacecraft to prevent the accumulation of space junk.

Appendix G: Microsoft Project for MS MicroEP Degree Plan

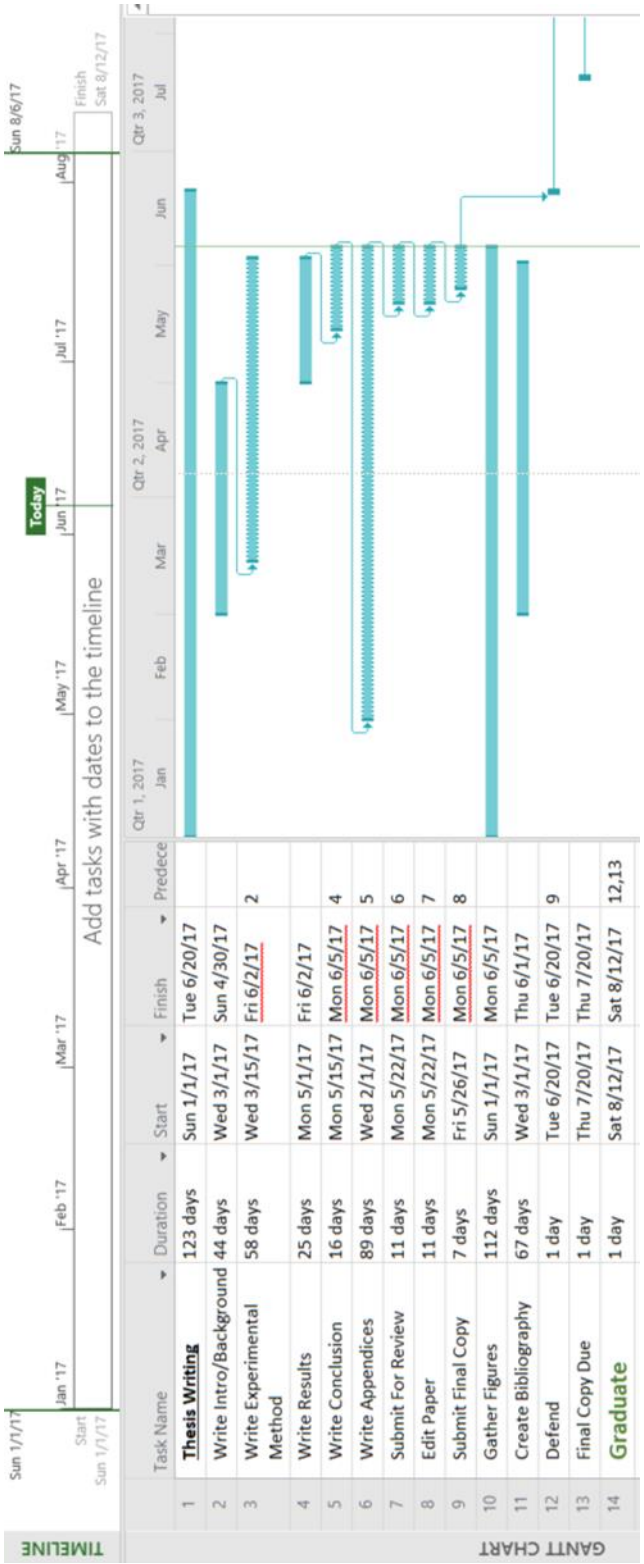

Appendix H: Identification of All Software Used in Research and Thesis Generation

Computer #1:

Model: Home built Windows PC

Windows Product ID: 00326-10856-05202-AA486

Location: Personal

Owner: Joshua Pennington

Computer #2:

Model: Huang lab built Windows PC

Windows Product ID: 00329-00000-00003-AA690

Location: ENRC 143

Owner: Huang lab

Software #1:

Name: Microsoft Office 2016

Purchased by: Joshua Pennington

Software #2:

Name: Matlab R2017a

Purchased by: Mechanical Engineering Department

Software #3:

Name: COMSOL 5.2

Purchased by: Microelectronics-Photonics Program

Appendix I: All Publications Published, Submitted, and Planned

Submitted

J.S. Pennington, A. Huang, “Simulation of Miniaturized Resonant Microwave Cavities with Applications to Advanced Space Propulsion.” Submitted to ASME 2017 IMECE Congress and Exposition.